Mechanistic and kinetic relevance of hydrogen and water in CO_2 hydrogenation on Cu-based catalysts

Ting C. Lin[a], Michelle A. Nolen[b, c], Carrie A. Farberow[c], Stephanie Kwon[b], and Aditya Bhan[a, 1]

[a]*Department of Chemical Engineering and Materials Science, University of Minnesota-Twin Cities, 421 Washington Ave. SE, Minneapolis, Minnesota 55455, United States*

[b]*Department of Chemical and Biological Engineering, Colorado School of Mines, 1613 Illinois St., Golden, Colorado 80401, United States*

[c]*Catalytic Carbon Transformation & Scale-Up Center, National Renewable Energy Laboratory, 15013 Denver W Pkwy., Golden, Colorado 80401, United States*

[1]Corresponding Author: E-mail: abhan@umn.edu; Fax: (+1) 612-626-7246

Keywords: CO_2, methanol, active site, coverage, adsorption energy, rate-determining step, mechanism

Abstract

We ally steady-state kinetics, kinetic isotope effects, and density functional theory (DFT) calculations to illustrate that Cu-based catalysts remain saturated by H-adatoms (H*) and molecular formic acid (HCOOH**) during CO_2 hydrogenation. High H* coverage under methanol synthesis conditions is evidenced by reverse water-gas shift (RWGS) rates that exhibit positive H_2 reaction orders only at $P_{H2} \lesssim 0.5$ bar, above which methanol synthesis and RWGS rates exhibit first and zeroth order dependence on P_{H2}, respectively. HCOOH** also accumulates on the surface with increasing P_{CO2} as informed by the Langmuir-type dependence on P_{CO2} (0.25–23 bar) for both methanol synthesis and RWGS. As both HCOOH** and H* have one H-atom per site occupied, the two species share the same P_{H2} dependence and give rise to CO_2 reaction orders that are independent of P_{H2}. Surface coverages determined based on kinetic analyses are further corroborated with DFT-derived adsorption energies that show favorable HCOOH** adsorbate-adsorbate interactions as well as repulsive interactions for bidentate formate (HCOO**) on H*-saturated surfaces. Methanol selectivity remains invariant with P_{CO2} and P_{CO} despite CO inhibiting reaction rates, thereby demonstrating the two reactions occur on the same active site. In contrast, water preferentially inhibits methanol synthesis rates, increases methanol synthesis H_2 reaction order from 1.0 to 1.5, and alters the H_2/D_2 kinetic isotope effect for methanol synthesis; the inhibitory effect of H_2O thus cannot be attributed to competitive adsorption alone but rather a change in the rate-determining step for methanol synthesis. The disparate kinetics of methanol synthesis and RWGS evince a branching pathway where methanol is formed from formates and CO is formed from carboxylates. The presented work thus identifies the relevant surface species, underscores the distinct catalytic role of water in branching methanol synthesis and RWGS

pathways, and, in doing so, details a mechanistic picture that yields predictable rates and reaction orders for both methanol synthesis and RWGS on Cu-based CO_2 hydrogenation catalysts.

1. Introduction

CO_2 removal and chemical conversion will likely play a critical role in clean energy technologies to create a low-carbon energy and industrial system for the future. By analogy to CO hydrogenation (Eq. 1), CO_2 hydrogenation (Eq. 2) promises the conversion of CO_2 to methanol, a platform C_1 chemical with the potential to replace current fossil fuels and establish a methanol-based energy economy[1,2]. Utilization of CO_2 instead of CO, however, is hampered by the need to activate strong C=O double bonds and the formation of H_2O as byproduct. Conventional methanol synthesis catalysts such as $Cu/ZnO/Al_2O_3$ also mediate reverse water-gas shift (RWGS; Eq. 3) to yield CO, thereby reducing methanol selectivity. A detailed mechanistic understanding of both methanol synthesis and RWGS reaction pathways during CO_2 hydrogenation on Cu-based catalysts is thus essential to provide information on reaction kinetics and to complement ongoing research on structure-function relationships identifying the roles of supports, properties of interfaces, and effects of nanoparticle geometries[3–7].

$$CO + 2H_2 \rightleftarrows CH_3OH \quad (1)$$

$$CO_2 + 3H_2 \rightleftarrows CH_3OH + H_2O \quad (2)$$

$$CO_2 + H_2 \rightleftarrows CO + H_2O \quad (3)$$

Early work by Chinchen et al.[8] relied on $^{14}CO_2$ to illustrate that methanol is mainly produced directly from CO_2 during CO_x hydrogenation on $Cu/ZnO/Al_2O_3$ with CO_2-to-CO ratios ranging from 0.0005 to 1.0. In contrast, Klier et al.[9] observed that 95% of the methanol yield corresponded to CO hydrogenation on Cu/ZnO at 75 atm (= 76 bar) with a feed composition of $CO_2/CO/H_2$ = 6/24/70, leading to the conclusion that CO hydrogenation is the dominant reaction pathway instead. While later studies by Chanchlani et al.[10] and Yang et al.[11] utilized kinetic measurements under varying CO_2-to-CO ratios and isotopic experiments at different temperatures

to demonstrate that the interplay between CO and CO_2 hydrogenation is condition-dependent (e.g., inlet composition and temperature), we previously leveraged reversibility-based arguments to show that the sequential RWGS + CO hydrogenation pathway to methanol is thermodynamically forbidden when using pure CO_2/H_2 feeds and $Cu/ZnO/Al_2O_3$ catalysts even as methanol synthesis from CO_2 reached reversibility values near 0.6 at a temperature of 523 K[12]. Vergara et al.[13] have adopted the same methodology in combination with spectroscopic techniques and arrived at consistent conclusions for CO_2 hydrogenation on $CuCeO_x/TiO_2$ catalysts. In other words, both methanol and CO appear to form directly from CO_2 under a CO-free feed following a branching reaction pathway involving distinct intermediates.

The general branching reaction mechanism provided by reversibility-based formalisms, however, neither specifies where the reaction pathway diverges nor enumerates the constitutive elementary steps – both aspects of CO_2 hydrogenation that research efforts have sought to address since the 1990s. Askgaard et al.[14] and Rasmussen et al.[15] used kinetic parameters derived from Cu single-crystal experiments and showed that microkinetic models with the formate pathway on Cu(100) for methanol synthesis and the redox mechanism (involving dissociative adsorption of CO_2 to yield CO*)[16,17] on Cu(111) for WGS/RWGS yield good agreement with experimentally measured turnover rates under various CO_2-to-CO ratios. These experimental data typically varied CO_2-to-CO ratio at constant CO_2+CO pressures and/or varied the total pressure but did not systematically modulate partial pressures of individual species. Recent computational[18–23] and experimental studies[11,20,24–26] focusing specifically on CO_2 hydrogenation have instead led to increasingly diverging views on the identity of the relevant reactive intermediate(s) for methanol synthesis and RWGS (e.g., formate (HCOO*) or carboxylate

(COOH*) pathways), the extent to which these intermediates are shared (i.e., where does the branching point occur), and the role of H_2O.

Elucidation of the mechanism and kinetics of heterogeneously catalyzed CO_2 hydrogenation is further predicated on evaluating the nature of the active sites. Due to the reducibility of ZnO, prior studies have argued that the nature of $Cu/ZnO/Al_2O_3$ depends on the reaction condition employed based on spectroscopic techniques and the use of probe molecules [5,27–29]. Novel synthetic procedures such as surface organometallic chemistry have also shown promotional effects for methanol synthesis and the involvement of alloys when reducible oxides such as ZnO and Ga_2O_3 are present as small domains in Cu-based catalysts[4]. While we have demonstrated through in situ methylene chloride titration that the active site density of $Cu/ZnO/Al_2O_3$ is invariant with H_2-to-CO_2 ratio[12], a proxy for the reduction potential experienced by the catalyst, the mechanistic role of ZnO remains unclear. In particular, Wang and Zhang[30] showed that the behavior of Cu/ZnO can best be described by a dual-site mechanism, where Cu and ZnO each require an independent site balance. Similarly, Portha et al.[31] found that their kinetic data on Cu/ZnO-based catalysts are well described by the microkinetic model established by Graaf et al.[32], which also employed one site for CO_2/CO adsorption and another for H_2 and H_2O adsorption. These dual-site mechanisms contrast microkinetic models that do not invoke two distinct sites[14,15], existing literature that demonstrates the rates of methanol synthesis from CO_x hydrogenation on Cu/ZnO remain proportional to the Cu surface area[33], and single crystal studies that suggest the role of ZnO is to stabilize Cu(110) facets based on comparable methanol synthesis rates observed on Cu(110) and Cu/ZnO[34]. Uncertainties regarding the nature of active sites and the relevant reactive intermediates are additionally complicated by the potential presence of dense adlayers under reaction conditions and coverage

effects that can lead to changes in reaction rates and pathways. Infrared studies as reported by Fisher and Bell[35] and Yang et al.[36] consistently illustrated the presence of formate-type species on Cu/SiO_2 catalysts under methanol synthesis conditions. Prior work on formic acid dehydrogenation on Cu/SiO_2 also demonstrated the ease for formates to saturate Cu surfaces, enabling bimolecular reaction pathways that exhibit lower activation barriers than unimolecular pathways[37]. Irrespective of the role of these surface formates (i.e., reactive intermediates or spectators), purported reaction mechanisms must accurately account for these coverages during catalysis.

Herein, we combine steady-state kinetics, isotopic experiments, and density functional theory (DFT) calculations to propose a novel mechanistic picture for CO_2 hydrogenation on Cu-based catalysts made possible by the high coverages of H* surface species under methanol synthesis conditions. The observed CO_2 and H_2 reaction orders for both methanol synthesis and RWGS on $Cu/ZnO/Al_2O_3$ and Cu/Al_2O_3 can be explained by a mechanism that involves one common active site for methanol synthesis and RWGS with the surface saturated by H* and HCOOH**. The preferential inhibition of methanol synthesis rates by H_2O, together with an increase in H_2 reaction order and a decrease in kinetic isotope effect (KIE) for only the methanol synthesis reaction with increasing P_{H2O}, evinces the presence of two elementary steps in the methanol synthesis catalytic cycle with variable rate controlling characteristics dependent on P_{H2O}. Disparate KIE values for methanol synthesis and RWGS along with the less pronounced H_2O inhibition for RWGS rates then show that methanol synthesis and RWGS involve distinct rate determining steps and reactive intermediates. The fact that these kinetic descriptions of CO_2 hydrogenation apply to both $Cu/ZnO/Al_2O_3$ and Cu/Al_2O_3 catalyst formulations renders it unlikely the incorporation of ZnO generates a new active site otherwise not present on Cu/Al_2O_3.

Altogether, the results of this work advance our current understanding of CO_2 hydrogenation by illustrating the disparate effect of water on the kinetics of competitive pathways for CO_2 hydrogenation mechanistically and highlighting the need for catalyst formulations that can promote formate conversion over carboxylate conversion to facilitate CO_2-to-fuel processes.

2. Methods

2.1. Catalyst preparation and testing

Commercial Cu/ZnO/Al_2O_3 (39.5 wt.% Cu, 20.5 wt.% Zn, 5.4 wt.% Al, 0.9 wt.% Mg, O bal.[12]; Alfa Aesar; product 45776; lot X03F006) and 13 wt.% Cu/Al_2O_3 (13.0 wt.% Cu, 40.6 wt.% Al, O bal.[12]; Sigma Aldrich; product 417971; batch MKCR8846) were crushed, pressed, and sieved to obtain aggregates that are 180–250 μm in diameter. These catalyst formulations were selected to evaluate the effects of ZnO addition on rates and selectivity of CO_2 hydrogenation to methanol on Cu-based catalysts. Catalyst samples (0.009–0.041 g) and sand diluent (Acros Organics; acid-washed with 2 M HNO_3 overnight and treated in flowing dry air at 1273 K for 10 h) in 1:10 by mass (catalyst:sand) for Cu/ZnO/Al_2O_3 were charged sequentially into a quarter-inch glass-lined stainless-steel reactor (Trajan Scientific; 08277028) with a quartz wool plug and a quartz rod as support. The reactor was shaken vigorously to mix the two components. The catalyst bed was then secured with a quartz wool plug and a quartz rod placed on top. The same procedure was followed for testing Cu/Al_2O_3 (0.072–0.120 g) except the dilution was 1:1 by mass (catalyst:sand). The reactor was resistively heated (National Element Inc.; FA120V120), with heating controlled by a PID controller (Watlow; Series 96) taking temperature measurements from a thermocouple (Omega; TJ36-CAXL-020U-12-SMPW-M) secured on the outer wall of the reactor tube near the catalyst bed. Stainless-steel gas carrier lines to and from the reactor were heated using heating tape (BriskHeat) and maintained at ca. 353 K using variable transformers

(Staco; 3PN1010B) to prevent condensation of CH_3OH and H_2O. System pressure was determined using electronic pressure transducers (Omega; PX309-1KG5V) connected to pressure meter devices (Omega; DP25B-E-A) and controlled manually using backpressure regulators (Enpro/Tescom; 26-1765-24-979). A Compact Profile Reactor (Reacnostics GmbH; [38,39]), which enables sampling gas composition axially in a tubular reactor, was also utilized with the same protocol as described above except with a lower pressure rating (pressure transducer: Omega PX309-500G5V; backpressure regulator: Enpro/Tescom; 44-2369-24-583) to facilitate space velocity experiments and delplot analysis for confirming CH_3OH and CO as the primary products of CO_2 hydrogenation on Cu-based catalysts (Sec. S1; Supporting information (SI)).

Gaseous species used for catalytic testing and their minimum purities are: He (Airgas; UHP; 99.999%), Ar (Airgas; Research Grade; 99.9997%), CO_2 (Airgas; Research Grade; 99.999%), H_2 (Airgas; UHP; 99.999%), and CO (Airgas; Semiconductor Grade; 99.997%) unless otherwise specified. Gas flow rates were modulated with mass flow controllers (Brooks Instrument; SLA5850), which were, in turn, controlled with a secondary electronic device (Brooks Instrument; 0260). High pressure H_2O (Fisher Scientific; HPLC Grade) and CH_3OH (Millipore Sigma; ACS Reagent Grade; ≥99.8%) co-feed experiments were performed using a high-pressure syringe pump (Harvard Apparatus; PHD Ultra XF; 70-3514) equipped with a stainless-steel syringe (Harvard Apparatus; 20 or 100 cm^3; 70-2251 or 70-2259) and controlled via a remote pump controller (Harvard Apparatus; 70-4401). Polymeric tubing was used for connection between the stainless-steel syringe and gas carrier lines to enable visual confirmation of liquid flow. Within the gas carrier line, a plug of quartz wool was placed at the liquid injection port to enhance liquid dispersion and mitigate flash vaporization. Furthermore, a stainless-steel mixing volume (50 cm^3; Swagelok; 304L-HDF4-50) was placed downstream of the liquid injection port

to attenuate pressure fluctuations and facilitate liquid flow stabilization. The syringe port is heated with heating tapes (BriskHeat), and its temperature was monitored with a thermocouple affixed to the outer wall and manually adjusted using the connected variable transformer (Staco; 3PN1010B) to achieve stable liquid vaporization.

Prior to introduction of reaction feed, catalyst samples were flushed with He (3.7×10^{-5} mol s^{-1}) for at least 6 h at ambient conditions and pretreated under 5% H_2/He (8.0×10^{-5} mol s^{-1}) at ambient pressure and 523 K (0.03 K s^{-1} from ambient) for 2 h. Catalyst reduction was confirmed from the evolution of H_2O as reported previously[12]. The reactor was then pressurized under flowing Ar to the desired reaction pressure while a separate stream with the desired feed composition was stabilized at the same pressure. Reaction was initiated by combining the Ar stream and the feed stream and flowing the mixed stream to the reactor such that Ar can be used as the internal standard. Composition of the effluent stream was determined using an online gas chromatograph (GC; Agilent; 7890A) equipped with PLOT U and Molsieve 5A columns along with a thermal conductivity detector (TCD) and a flame ionization detector (FID) connected in series to allow cross referencing between the two detectors and quantification of methanol via FID despite Ar being only sensed through TCD, yielding higher sensitivity. The relative response factors were established based on mixtures of known compositions. Conversion, selectivity, and overall reversibility are defined as

$$X_{CO_2} = \frac{F_{CH_3OH} + F_{CO}}{F_{CO_2} + F_{CH_3OH} + F_{CO}} = X_{CO_2,\mathrm{MeOH}} + X_{CO_2,\mathrm{RWGS}} \tag{4}$$

$$S_{\mathrm{MeOH}} = \frac{F_{CH_3OH}}{F_{CH_3OH} + F_{CO}} \tag{5}$$

$$Z_{\mathrm{ov}} = \frac{1}{K_{\mathrm{eq}}} \prod_j P_j^{\nu_{j,\mathrm{ov}}} = \frac{1}{K_{\mathrm{eq}}} \prod_j \left(\frac{F_j}{F_{\mathrm{tot}}} P_{\mathrm{tot}}\right)^{\nu_{j,\mathrm{ov}}} \tag{6}$$

where F_j is the molar flow rate of species j, P_j is the partial pressure of species j, $\nu_{j,\mathrm{ov}}$ is the stoichiometric coefficient of species j in the overall reaction, and K_{eq} is the equilibrium constant of the overall reaction evaluated based on temperature-corrected reaction enthalpy and entropy[12,40]. For experiments with product cofeed (e.g., CO co-feed), only the products formed from CO_2 (calculated based on F_{H_2O}) were used to determine conversion and selectivity, but the total product flow rates (co-feed + produced) were used to calculate reversibility. Due to inaccuracies of TCD in quantifying H_2 and H_2O and the high sensitivity of Z_{ov} on the flow rates of these species, F_{H_2} and F_{H_2O} were determined based on the stoichiometry of the reactions and the inlet composition for calculating reversibility (except for CO and methanol co-feed experiments where F_{H_2O} is as measured) but are reported as measured elsewhere unless otherwise specified. Trace methyl formate and dimethyl ether were detected under certain conditions, but only at concentrations estimated to be approximately two orders of magnitude lower than that for methanol based on GC peak areas. Hence, these species were not included in the calculations outlined above.

Rate measurements are devoid of limitations from heat and mass transfer as previously confirmed based on comparable rates obtained from cases with and without sand diluent and from cases with varying catalyst aggregate sizes (125–180 μm vs 180–250 μm in diameter) under similar reaction conditions[12]. Herein, all rates reported on $Cu/ZnO/Al_2O_3$ were normalized by the active site density quantified using in situ CH_2Cl_2 titration[12,41] while all rates reported on Cu/Al_2O_3 were normalized by the active site density quantified based on ex situ N_2O reactive frontal chromatography[12,42]. Parameter estimation and microkinetic modeling using the measured rates were performed with AthenaVisual Plus (v21.1; AthenaVisual, Inc.) following Bayesian statistics.

2.2. Kinetic isotope effect

H_2/D_2 kinetic isotope effect (KIE) under dry conditions for methanol synthesis and RWGS were measured by switching H_2 with D_2 (Matheson Gas; UHP; 99.995% chemical purity excluding H_2 and HD; 99.7% isotopic enrichment) on stream to mitigate variations in rates due to errors in the amount of catalyst charged. Steady-state rates were first measured under CO_2/H_2, after which H_2 was replaced by D_2 for steady-state rate measurements under CO_2/D_2. As there are no other sources of H, observed KIE at steady state should be devoid of effects from H/D scrambling. Following the same reason, KIE under wet conditions was evaluated using feeds of $H_2/CO_2/H_2O$ and $D_2/CO_2/D_2O$ (D_2O; Cambridge Isotope Laboratories, Inc.; 99.5% chemical purity; 99.9% isotopic enrichment) as co-processing D_2 with H_2O would likely lead to significant H/D scrambling. Separate catalyst loadings were utilized to compare rates under wet conditions due to difficulties in switching pressurized liquid injection between H_2O and D_2O on stream; comparable rates at a reference condition (P_{CO2} = 4.7 bar; H_2:CO_2 = 1:1) were confirmed for the catalyst beds used. In both wet and dry isotopic experiments, the FID response factors of CD_3OD and CH_3OH were presumed to be equal based on prior literature demonstrating equal FID response for hydrocarbons with and without deuterium substitution[43]. This assumption was not made for the TCD response factors of CD_3OD and CH_3OH as deuterium substitution may change the thermal conductivity[44].

2.3. Computational methods

DFT calculations were performed using the Vienna Ab initio Simulation Package (VASP)[45,46] and predicted geometries were visualized using VESTA[47]. The generalized gradient approximation (GGA) with the Perdew-Burke-Ernzerhof (PBE) functional[48] was used to approximate the exchange-correlation energy, which has been previously used in the literature

to assess CO/CO_2 hydrogenation routes on Cu surfaces[49–51]. The DFT-D3 method of Grimme et al.[52] was applied to account for dispersion forces that describe weak interactions between adsorbates and transition-metal surfaces. Electron-ion interactions were described using the projector augmented-wave (PAW) method[53] with electronic wave functions expanded in a plane-wave basis set with a kinetic energy cutoff of 400 eV. The electronic convergence criterion was set to 10^{-6} eV between successive electronic relaxation steps, while ionic convergence was set to occur when the Hellmann-Feynman forces acting upon each atom fell below 0.02 eV/Å. The thermodynamically favored (111) facet of Cu[54] was modeled with a 4×4×5 periodic unit cell and at least 10 Å of vacuum between successive slabs in the z direction. The Monkhorst-Pack k-point mesh of 4×4×1 were used for sampling of the Brillouin zone[55]. While prior reports have ascribed unique roles to Cu/Zn interfaces[29,56–58], our experimental findings demonstrate that ZnO does not generate a new active site based on similar kinetics observed on both $Cu/ZnO/Al_2O_3$ and Cu/Al_2O_3 (*vide infra*). We thus focused our simulations on Cu(111) to obtain results that are applicable to both $Cu/ZnO/Al_2O_3$ and Cu/Al_2O_3. The choice of Cu(111) is further based on the assumption that the most thermodynamically stable Cu(111) facet dominates the surface given the relatively high Cu loading employed in this work (>10 wt.% Cu; Sec. 2.1).

Energies of bound intermediates were probed on the four distinct high-symmetry sites of the (111) surface (top, bridge, fcc, and hcp; Sec. S2; SI). Only the lowest-energy values are reported. Average adsorption energies on Cu(111) surfaces were calculated as follows:

$$E_{\mathrm{ads,avg}} = \frac{E_{\mathrm{n-tot}} - E_{\mathrm{slab}} - nE_{\mathrm{gas-phase}}}{n} \tag{7}$$

$E_{\mathrm{n-tot}}$ is the total energy of n adsorbates on a Cu(111) slab, E_{slab} is the energy of the Cu(111) slab, and $E_{\mathrm{gas-phase}}$ is the gas-phase energy of the adsorbate. The adsorption energies of (CO_2+H_2)-derived species (carboxylate (COOH*+H*), formate (HCOO**+H*), molecular formic

acid (HCOOH**)), were calculated with respect to gas-phase energies of CO_2 and H_2. The adsorption energies of carboxylate and formate species were calculated in the presence of a single co-adsorbed hydrogen to maintain an atom balance with CO_2+H_2. The adsorption energies of CO* and H* were referenced to CO(g) and ½H_2(g), respectively, and the adsorption energies of HCO* and COH* were referenced to CO(g) + ½H_2(g). For adsorption energies on H*-covered surfaces,

$$E_{\text{ads}} = E_{tot,iH^*} - E_{\text{slab},iH^*} - E_{\text{gas-phase}} \quad (8)$$

E_{tot,iH^*} is the total energy of the adsorbate on a Cu(111) slab with i spectator H*-atoms, and E_{slab,iH^*} is the energy of a slab with i H*-atoms. The differential adsorption energy ($E_{\text{ads,diff}}$) of formic acid was calculated by taking the energetic difference between 0.0625 ML increments of formic acid coverage:

$$E_{\text{ads,diff}} = E_{\text{tot},jHCOOH^{**}} - E_{\text{slab},(j-1)HCOOH^{**}} - E_{\text{gas-phase}} \quad (9)$$

$E_{\text{tot},jHCOOH^{**}}$ is the total energy of j adsorbed formic acid molecules on the Cu slab, $E_{\text{slab},(j-1)HCOOH^{**}}$ is the energy of j-1 adsorbed formic acid molecules on a Cu slab, and $E_{\text{gas-phase}}$ is the gas-phase energy of CO_2 and H_2.

The nudged elastic band (NEB) method[59] was used to search for transition-state (TS) structures; initial and final structures were connected with at least four images. At least three different NEB calculations were tested for a single transition-state search with an energy convergence criterion of 10^{-6} eV and a force convergence criterion of 0.05 eV/Å for each image. The converged NEB calculations were used to generate inputs for the dimer method[60] by selecting two images near the saddle point[61]. The force convergence criterion for the dimer calculations was 0.05 eV/Å and the energy convergence criterion was 10^{-6} eV. Isolated transition-state structures were confirmed by the presence of a single imaginary vibrational frequency along the reaction coordinate.

Vibrational frequencies were calculated using a finite-difference approximation of the Hessian matrix[62], where all bound intermediates were fully relaxed during the vibrational analysis, and all metal atoms remained fixed. The relative infrared intensity of each vibrational mode was approximated using a code developed for this purpose[63]. The infrared intensity is proportional to the square of the directional derivative of the dipole moment ($\partial\mu_z/\partial Q_i$), where μ_z is the dipole moment in the z direction (perpendicular to the slab) and Q_i is the distance of perturbation for each mode[64]. Lorentzian broadening was applied to each peak to aid with the visualization of the calculated spectra. An arbitrary width of 20 cm^{-1} was applied. For deuterated species, the mass-weighted Hessian matrix was modified to reflect the mass of deuterium (2 amu) rather than hydrogen (1 amu). The frequencies of relevant bound and gas-phase intermediates were used to calculate enthalpic ($\Delta H^{\ddagger}$) and entropic ($\Delta S^{\ddagger}$) components of the Gibbs free activation energy ($\Delta G^{\ddagger}$) from statistical mechanical formalisms[65]. These thermodynamic values were used to calculate rate constants of elementary steps and the corresponding KIE.

3. Results and discussion

3.1. Number of distinct active sites and species coverages under reaction conditions

Questions regarding the active sites for CO_2 hydrogenation on Cu-based catalysts are two-fold: (i) do Cu-based catalysts contain more than one type of active site, and (ii) which species, if any, occupies the active sites during catalytic reaction? Regarding the former, we previously utilized in situ methylene chloride titration to demonstrate that the active site density and, consequently, the extent of structural changes for $Cu/ZnO/Al_2O_3$ catalysts remain largely invariant with reduction potential and showed identical apparent H_2 and CO_2 reaction orders for CO_2 hydrogenation on $Cu/ZnO/Al_2O_3$ and Cu/Al_2O_3 catalyst formulations[12]. In Section 3.3, we further supplement these findings with the observation that H_2O preferentially inhibits methanol

synthesis rates and increases methanol synthesis H_2 reaction order on both $Cu/ZnO/Al_2O_3$ and Cu/Al_2O_3. These results together indicate that the addition of ZnO does not generate unique active sites for methanol synthesis that are unavailable on Cu/Al_2O_3 despite reaction on $Cu/ZnO/Al_2O_3$ exhibiting higher methanol selectivity. The presence of only one type of active site on $Cu/ZnO/Al_2O_3$ is further evidenced by the invariance in methanol selectivity with CO_2 and CO partial pressures (Figs. 1 and 2). If methanol synthesis and RWGS occur on distinct active sites, coverages of CO_2- and CO- derived surface intermediates on these distinct active sites should exhibit disparate dependence on P_{CO2} on P_{CO}, leading to significant changes in methanol selectivity with modulations in P_{CO2} and P_{CO}. The absence of such variations in methanol selectivity as shown in Figures 1 and 2, therefore, also shows that there is a common active site for methanol synthesis and RWGS such that coverages of CO_2- and CO-derived surface species do not preferentially influence one reaction pathway over the other.

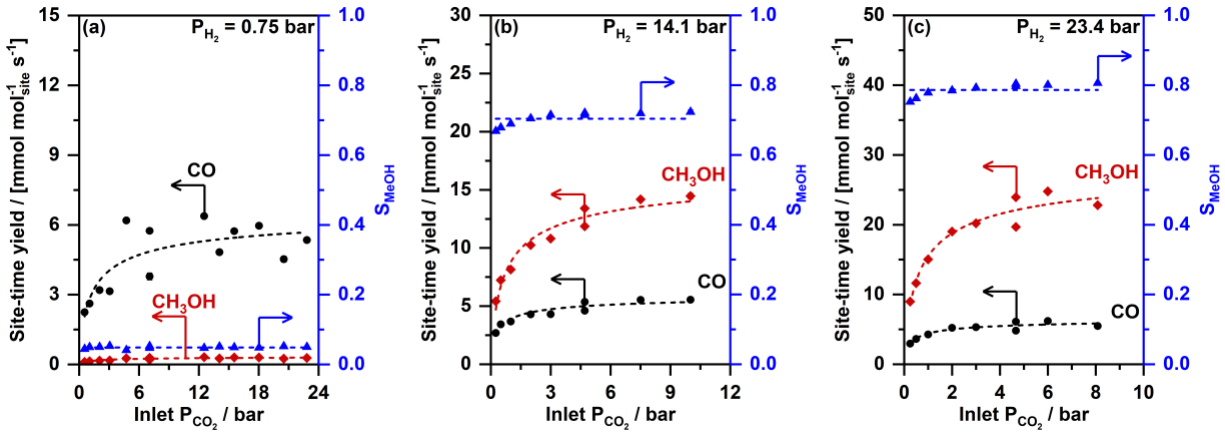

Figure 1. Methanol site-time yield (red), CO site-time yield (black), and methanol selectivity (blue) on $Cu/ZnO/Al_2O_3$ at 523 K as a function of P_{CO2} at (a) P_{H2} = 0.75 bar [H_2:(He+CO_2):Ar = 1:24.2:10.6 or 1:31.3:3.6; 3.8×10^{-4} mol s^{-1} total; X_{CO_2} = 0.00043–0.0079; $Z_{ov,MeOH}$ < 0.16, $Z_{ov,RWGS}$ < 0.0040], (b) P_{H2} = 14.1 bar [H_2:(He+CO_2):Ar = 1:1.1:0.07; 2.9×10^{-4} mol s^{-1} total; X_{CO_2} = 0.0066–0.090; $Z_{ov,MeOH}$ < 0.026, $Z_{ov,RWGS}$ < 0.0055], and (c) P_{H2} = 23.4 bar [H_2:(He+CO_2):Ar = 1:0.35:0.11; 3.1×10^{-4} mol s^{-1} total; X_{CO_2} = 0.0070–0.081; $Z_{ov,MeOH}$ < 0.0055, $Z_{ov,RWGS}$ < 0.0021]. Trendlines are shown to guide the eye. Error bars reflect standard deviations determined from replicate GC injections.

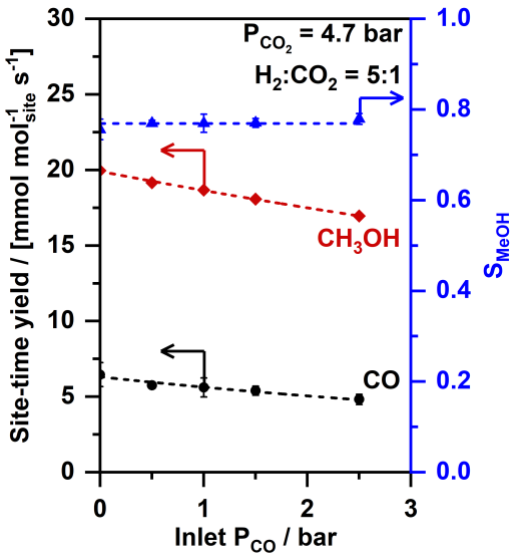

Figure 2. Methanol site-time yield (red), CO site-time yield (black), and methanol selectivity (blue) on Cu/ZnO/Al_2O_3 at 523 K as a function of P_{CO} at P_{CO2} = 4.7 bar [H_2:CO_2:Ar:(He+CO) = 5:1:0.45:2.3; 2.5×10^{-4} mol s^{-1} total; X_{CO_2} = 0.015–0.019; $Z_{ov,MeOH}$ < 0.0045, $Z_{ov,RWGS}$ < 0.15]. CO site-time yields were determined by subtracting methanol site-time yield from H_2O site-time yield. Trendlines are shown to guide the eye. Error bars reflect standard deviations determined from replicate GC injections.

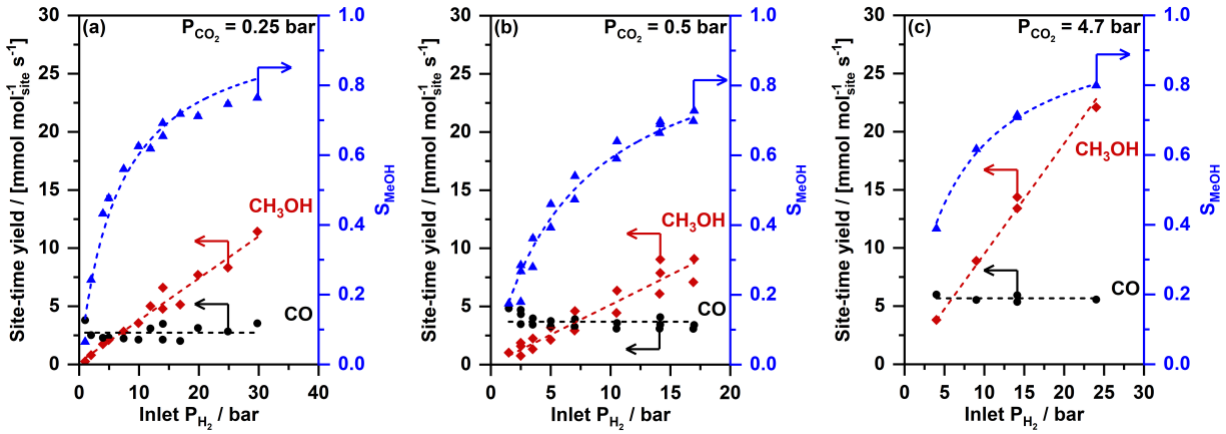

Figure 3. Methanol site-time yield (red), CO site-time yield (black), and methanol selectivity (blue) on Cu/ZnO/Al_2O_3 at 523 K as a function of P_{H2} at (a) P_{CO2} = 0.25 bar [(He+Ar+H_2):CO_2 = (80.4–131.9):1; 1.5×10^{-4}–4.2×10^{-4} mol s^{-1} total; X_{CO_2} = 0.016–0.10; $Z_{ov,MeOH}$ < 0.58, $Z_{ov,RWGS}$ < 0.015], (b) P_{CO2} = 0.5 bar [(He+H_2):CO_2:Ar = 6.8:1:0.24 or 37.8:1:1.2; 3.0×10^{-4} mol s^{-1} total; X_{CO_2} = 0.012–0.096; $Z_{ov,MeOH}$ < 0.47, $Z_{ov,RWGS}$ < 0.028], and (c) P_{CO2} = 4.7 bar [(He+H_2):CO_2:Ar = 5.4:1:0.21; 2.9×10^{-4} mol s^{-1} total; X_{CO_2} = 0.0067–0.019; $Z_{ov,MeOH}$ < 0.058, $Z_{ov,RWGS}$ < 0.0030]. Trendlines are shown to guide the eye. Error bars reflect standard deviations determined from replicate GC injections.

To identify the most abundant surface intermediates (MASIs) (question (ii)), we now consider the apparent reaction orders. Both methanol synthesis and RWGS exhibit Langmuir-type dependence on P_{CO2} across P_{H2} = 0.75–23.4 bar (Fig. 1). Conversely, methanol synthesis and RWGS exhibit persistent first and zeroth order dependence on P_{H2} across P_{CO2} = 0.25–4.7 bar (Fig. 3). We note that while reaction rates are weakly inhibited by CO (Fig. 2), this inhibition is only appreciable at P_{CO} higher than those present during experiments with pure CO_2/H_2 feed in this study (e.g., effluent P_{CO} is below 0.02 bar for all points shown in Fig. 1b). CO inhibition further does not influence methanol selectivity, indicating that this inhibition stems from competitive adsorption between surface species derived from CO and those derived from CO_2 and H_2 such that methanol synthesis and RWGS rates are equally inhibited by CO. In contrast, H_2O preferentially influences methanol synthesis rates and reaction orders through phenomena beyond just competitive adsorption (*vide infra*; Sec. 3.3). No inhibition by CH_3OH was observed at relevant pressures of CH_3OH (Sec. S3; SI). We thus first focus on identifying H_2- and CO_2-derived surface intermediates to explicate the apparent H_2 and CO_2 reaction orders and reserve discussion on the effects of H_2O and CO to Section 3.3.

The observations that the apparent CO_2 reaction orders are independent of P_{H2} (Fig. 1) and that the apparent H_2 reaction orders are independent of P_{CO2} (Fig. 3) together suggest a rate expression with the functional form of

$$\frac{r}{[L]} \propto \frac{P_{H_2}^{\gamma} P_{CO_2}}{1 + K P_{CO_2}} \tag{10}$$

where γ is 1 for methanol synthesis and 0 for RWGS to reflect the observed H_2 reaction orders. Equation 10, as written, is purely empirical, does not readily reflect appreciable coverages by formate-type species previously observed through infrared studies[35,36,66], and, therefore, must instead be a simplified functional form of the intrinsic rate expression derived from constitutive

elementary steps and site balances. Namely, the commonly proposed dual-site mechanism[30–32] where H_2 activation occurs on one site while CO_2 conversion occurs on another site can yield rate expressions mathematically equivalent to Equation 10 under the condition that the site responsible for H_2 activation remains saturated with surface H* species (Eq. 11).

$$\frac{r}{[L]} \propto \frac{P_{H_2}^{\gamma'} P_{CO_2}}{\underbrace{\left(1+\sqrt{K_{H_2}P_{H_2}}\right)}_{\text{site 1}}\underbrace{\left(1+KP_{CO_2}\right)}_{\text{site 2}}} \approx \frac{P_{H_2}^{\gamma'} P_{CO_2}}{\left(\sqrt{K_{H_2}P_{H_2}}\right)\left(1+KP_{CO_2}\right)} \tag{11}$$

Here, γ' is 1.5 for methanol synthesis and 0.5 for RWGS to reflect the observed H_2 reaction orders. This mechanism, however, again assumes that the site responsible for CO_2 conversion (the second factor in the denominator) is either bare or saturated with CO_2* and cannot account for the presence of partially hydrogenated intermediates (e.g., surface formates), contradicting our expectation that CO_2 binds weakly on transition metal surfaces and prior spectroscopic studies[35,36] that have detected strongly bound formates.

In essence, the observed Langmuir-type dependence on P_{CO2} demonstrates the presence of at least two terms in the site balance out of which only one is derived from CO_2 such that the CO_2-derived contribution dominates the surface at high P_{CO2} (zeroth-order regime) and the non-CO_2-derived contribution dominates the surface at low P_{CO2} (first-order regime). The independence of CO_2 reaction orders on P_{H2} (Fig. 1), in turn, requires these two terms to have the same dependence on P_{H2} such that changes in P_{H2} do not alter their relative coverages and, consequently, the CO_2 reaction orders. From a stoichiometry perspective, these inferences necessitate the presence of surface species that have the same number of H-atoms per site with different numbers of CO_2, a constraint satisfied with H* (one H per site) and a surface species derived from CO_2+$n$$H_2$ that occupies $2n$ sites (also one H per site) being the MASIs for methanol synthesis and RWGS. From a mathematical perspective, we first let I^{2n}* denote the (CO_2+$n$$H_2$)-derived intermediate that

occupies $2n$ sites. Under the typical condition that the MASIs are formed from fast and equilibrated steps, we write the following equilibrium relationships where K_I is the lumped equilibrium constant for the reaction between CO_2(g) and $(2n)$H* to form I^{2n}* while K_I/K_{CO_2} is the lumped equilibrium constant for the surface reaction between CO_2* and $(2n)$H* to form I^{2n}* (Eqs. 12–14).

$$H_2 + 2* \rightleftarrows 2H^* \qquad K_{\text{eq}} = K_{H_2} \tag{12}$$

$$CO_2 + * \rightleftarrows CO_2^* \qquad K_{\text{eq}} = K_{CO_2} \tag{13}$$

$$CO_2 + (2n)H^* \rightleftarrows I^{2n*} \qquad K_{\text{eq}} = K_I \tag{14a}$$

$$CO_2^* + (2n)H^* \rightleftarrows I^{2n*} + * \qquad K_{\text{eq}} = K_I/K_{CO_2} \tag{14b}$$

The site balance for a surface saturated with H* and I^{2n}* is accordingly

$$[L] = [H^*] + 2n[I^{2n*}] \tag{15}$$

While we can directly solve the site balance (Eq. 15) for $[*]/[L]$ using Equations 12 to 14, we note that the stoichiometry enables us to solve the site balance more simply on a H* basis. This mathematical simplification is a direct consequence of the surface being H*-saturated under reaction conditions such that CO_2 effectively adsorbs by reacting with $(2n)$H* to form I^{2n}* (K_I; Eq. 14a). From Equation 14a, we know that

$$K_I = \frac{[I^{2n*}]}{P_{CO_2}[H^*]^{2n}/[L]^{2n-1}} \Rightarrow [I^{2n*}] = \frac{K_I P_{CO_2}[H^*]^{2n}}{[L]^{2n-1}} \tag{16}$$

where the $[L]^{2n-1}$ term in the denominator is a statistical factor for normalization as the forward reaction shown in Equation 14a involves $2n$ surface species while the reverse reaction only involves one surface species. Substituting Equation 16 into Equation 15 now results in a site balance on a per H* basis,

$$[L] = [H^*] + \frac{2nK_I P_{CO_2}[H^*]^{2n}}{[L]^{2n-1}} \Rightarrow 1 = \left(\frac{[H^*]}{[L]}\right) + 2nK_I P_{CO_2}\left(\frac{[H^*]}{[L]}\right)^{2n} \quad (17)$$

where we can define $\frac{1}{f(P_{CO_2})}$ as the solution for $[H^*]/[L]$; $f(CO_2)$ thus accordingly accounts for the coverages of surface species on a per H* basis.

$$\frac{1}{f(P_{CO_2})} = \frac{[H^*]}{[L]} \quad (18)$$

Finally, Equation 12 enables us to solve for $[*]/[L]$ (Eqs. 19 and 20) and show that the stoichiometry of the surface species alone can decouple P_{H2} and P_{CO2} dependencies as factor multiples, mirroring the functional form of the empirical rate expression (Eq. 10).

$$K_{H_2} = \frac{[H^*]^2}{P_{H_2}[*]^2} \Rightarrow [H^*] = \sqrt{K_{H_2}P_{H_2}}[*] \quad (19)$$

$$\frac{[*]}{[L]} = \frac{1}{\sqrt{K_{H_2}P_{H_2}}}\left[\frac{1}{f(P_{CO_2})}\right] \quad (20)$$

The fact that bare sites do not contribute to the site balance may seem unexpected due to the first-order dependence on P_{H2} for methanol synthesis (Fig. 3), which typically suggests a dearth of H* species. The persistent zeroth-order dependence on P_{H2} for RWGS (Fig. 3), however, demonstrates that the surface should be H*-saturated. Indeed, positive order dependence on P_{H2} for RWGS can only be observed at P_{H2} below 0.5 bar, much lower than P_{H2} at conditions relevant for methanol synthesis (Fig. 4). The difference in H_2 reaction orders for methanol synthesis and RWGS then arises simply because the rate-determining steps for the two reactions are distinct (more in Sec. 3.4), with the intermediate(s) reacting in the methanol synthesis rate-determining step having two additional H atoms relative to that for RWGS such that methanol synthesis exhibits a persistent first order H_2 dependence even under elevated P_{H2} (Fig. 3).

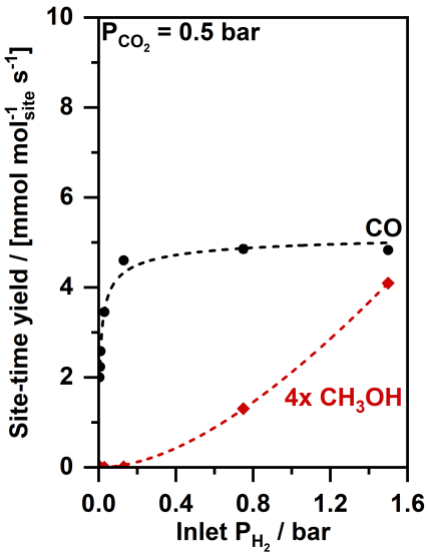

Figure 4. Methanol (red) and CO (black) site-time yields on $Cu/ZnO/Al_2O_3$ at 523 K under reverse water-gas shift conditions (P_{H2} and P_{CO2} ~0.5 bar) as a function of P_{H2} at P_{CO2} = 0.5 bar [$(He+H_2):CO_2:Ar$ = 6.8:1:0.24 ; 3.0×10^{-4} mol s^{-1} total; X_{CO_2} = 0.0030–0.012; $Z_{\mathrm{ov,MeOH}} < 0.46$, $Z_{\mathrm{ov,RWGS}} < 0.25$]. Trendlines are shown to guide the eye. Error bars reflect standard deviations determined from replicate GC injections.

3.2. Stoichiometry and identity of the I^{2n*} reactive intermediate

Relating the site balance (Eq. 20) to the empirical rate expression (Eq. 10) is predicated on identifying I^{2n*}. The constraint on the number of H atoms in the MASIs as outlined in the preceding section establishes the number of H atoms per site but does not specify the ratio of H atoms to CO_2 in I^{2n*}. To quantify n, we evaluate the number of CO_2 per site occupied as an indirect approach to probe the stoichiometry between H and CO_2 for this intermediate species. With all adsorption and desorption steps presumed to be equilibrated, the rate-determining steps for methanol synthesis and RWGS may involve C–O cleavage, C–H formation, or O–H formation (*vide infra*; Scheme 3). Each of these elementary steps either produces or consumes two surface species and, consequently, requires two active sites, leading to rate expressions that have their denominators raised to the power of two. Moreover, since both the reactants and products are C_1 species, we surmise the rate-determining step should only involve one CO_2, indicating the numerator of the rate expressions should be proportional to P_{CO2}. While prior literature has suggested the involvement of methyl

formate[67,68], a C_2 species, as an intermediate for methanol synthesis, proposed RWGS mechanisms (formate, carboxylate, or redox) do not proceed through C_2 intermediates. The involvement of methyl formate in the rate-determining step for methanol synthesis will therefore lead to disparate CO_2 reaction orders for methanol synthesis and RWGS, in contrast to the data reported in Figure 1.

Accordingly, if I^{2n*} only occupies one site (n = 0.5; $I^{2n*} = I^{*}$), it should exhibit the atomic stoichiometry equivalent to that of monodentate formate (HCOO*) leading to a rate expression given by

$$\frac{1}{f\left(P_{CO_2}\right)} = \frac{1}{1 + K_I P_{CO_2}} \Rightarrow \frac{r}{[L]} \propto \frac{P_{H_2}^{\gamma''} P_{CO_2}}{K_{H_2} P_{H_2} \left(1 + K_I P_{CO_2}\right)^2} \tag{21}$$

where γ'' is 2 for methanol synthesis and 1 for RWGS (derivation in Sec. S4; SI). Equation 21, however, results in a negative-first-order dependence on P_{CO2} at high CO_2 partial pressures, which is not observed (Fig. 1). This demonstrates that I^{2n*} should instead occupy two sites (n = 1; $I^{2n*} = I^{2*}$), exhibit atomic stoichiometry equivalent to that of molecular formic acid (HCOOH**), and results in a rate expression of the form

$$\frac{1}{f\left(P_{CO_2}\right)} = \frac{2}{1 + \sqrt{1 + 8K_I P_{CO_2}}} \Rightarrow \frac{r}{[L]} \propto \frac{4P_{H_2}^{\gamma''} P_{CO_2}}{K_{H_2} P_{H_2} \left(1 + \sqrt{1 + 8K_I P_{CO_2}}\right)^2} \tag{22}$$

which now resembles Equation 10, where the H_2 reaction order remains constant and the CO_2 reaction order transitions from first order to zeroth order with increasing P_{CO2} (derivation in Sec. S5; SI). The square root term in the denominator (site balance) manifests precisely because I^{2*} occupies two active sites. The value of γ'' is again 2 for methanol synthesis and 1 for RWGS to yield the observed first and zeroth H_2 reaction orders (Fig. 3), showing that the intermediate(s)

reacting in the rate-determining steps for methanol synthesis and RWGS should have four and two H-atoms, respectively.

Dioxymethylene (H_2COO**), dihydroxymethylidene (HOCOH**), and molecular formic acid (HCOOH**) each exhibit the stoichiometry of one CO_2 + one H_2 and can potentially occupy two active sites (Figs. 5a–c). Our DFT-derived adsorption energies show that HCOOH** is the most stable species among these candidates on Cu(111) with a significant H* coverage (0.5 ML) as expected under reaction conditions (HCOOH** = -66 kJ mol^{-1}, H_2COO** = +25 kJ mol^{-1}, and HOCOH* = +24 kJ mol^{-1}, all uniformly referenced to CO_2(g) + H_2(g)). To further differentiate between these surface species, we juxtapose DFT-derived infrared (IR) spectra of these species on Cu(111) with 0.5 ML H* coverage (Fig. 5d) against the experimental IR spectrum for steady-state CO_2+H_2 reactions on Cu/SiO_2 as reported by Yang et al.[36] (6 bar P_{tot}; H_2:CO_2 = 3:1; 353 K; 10 wt.% Cu/SiO_2; Fig. 5e). From Figures 5d and 5e, H_2COO** can be ruled out based on the absence of predicted IR bands across the 1230 to 1730 cm^{-1} region where IR bands were observed experimentally. Comparing HOCOH** and HCOOH**, only HCOOH** exhibits a feature at 1660 cm^{-1} which may correspond to the 1580 cm^{-1} band in the experimental IR spectrum. We note that the DFT methods utilized in this work (PBE-D3, PAW potentials) typically overestimate fundamental vibrational frequencies; applying the recommended scaling factor (0.988)[69] lowers the wavenumber to 1640 cm^{-1}, improving agreement with experimental values. Our conclusion of the presence of HCOOH** species based on steady-state kinetics, reaction orders, and DFT-derived adsorption energies thus does not necessarily contradict prior infrared studies given the controversial origin of the IR band at 1580 cm^{-1}[36,37,70,71] and the absence of an infrared band at 1580 cm^{-1} in our DFT-derived IR spectra for bidentate formate (HCOO**) on bare Cu(111) and Cu(111) with 0.5 ML H* coverage (Sec. S6; SI). The HCOO*/H* complex, formed from the

interaction between monodentate formate (HCOO*) and a vicinal H*, was additionally evaluated as an alternative to HCOOH** for the most abundant CO_2-derived surface intermediate. Interaction between HCOO* and H*, however, is unfavorable as geometry optimization of HCOO* on Cu(111) with 0.5 ML H* coverage consistently orients HCOO* away from neighboring H* species, demonstrating that the HCOO*/H* complex is unlikely to be present (Sec. S7; SI). We further note that the experimental IR band at 1350 cm^{-1} is commonly assigned to the symmetric vibrational mode of HCOO**. As HCOO** is a precursor to HCOOH** (Sec. 3.5), HCOO** may be present in small amounts such that it does not manifest in the site balance but does result in an IR feature. Alternatively, there may be a fixed amount of refractory HCOO** present[37,72]; our kinetic analyses will then remain applicable to reaction on the *active* sites free of these refractory HCOO** species. While our experimental observations cannot rule out the presence of inactive HCOO**, we show in the following that HCOO** exhibits unfavorable interactions with surface H* through DFT-derived adsorption energies to evaluate adsorbate-adsorbate interactions.

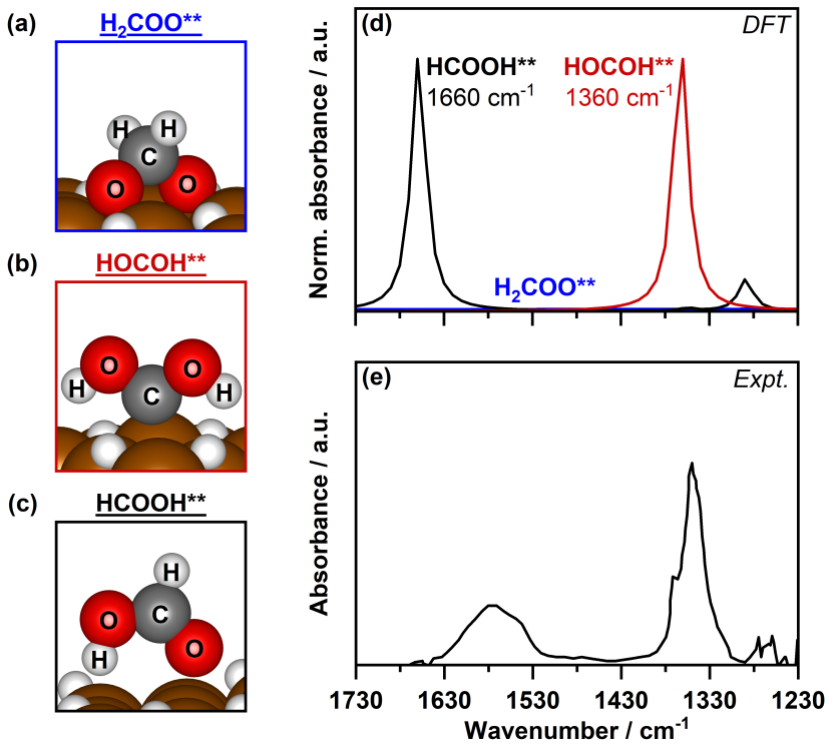

Figure 5. DFT-derived geometries of (a) H_2COO**, (b) HOCOH**, and (c) HCOOH** on Cu(111) with 0.5 ML H* coverage. (d) Normalized DFT-derived infrared spectra for the three species on Cu(111) with 0.5 ML H* coverage and (e) experimental in situ infrared spectra (6 bar P_{tot}; H_2:CO_2 = 3:1; 353 K; 10 wt.% Cu/SiO_2) reproduced with permission from reference [36]. Copyright 2008 Springer Nature.

Prior DFT studies[18,73–75] have reported the abundance of HCOO** during methanol synthesis based on its high stability on clean Cu surfaces and steady-state coverages predicted from mean-field microkinetic models. Although HCOO** (with a co-adsorbed H* to maintain an atom balance with gas-phase reactants) is more stable than HCOOH** on bare Cu surfaces (DFT-derived adsorption energy of -107 kJ mol^{-1} for HCOO**+H* vs -75 kJ mol^{-1} for HCOOH**), significant H* coverages impose repulsive interactions that destabilize HCOO**, as shown through DFT-derived adsorption energy that increases with increasing H* coverage (Fig. 6a). In contrast, HCOOH** is not influenced by H* coverage, rendering it the most stable surface intermediate under high H* coverages ($\gtrsim$ 0.6 ML H*; Fig. 6a). HCOOH** further benefits from adsorbate-adsorbate H-bonding interactions, resulting in HCOOH** differential adsorption energy

that becomes more negative above ~0.25 ML HCOOH** (Fig. S6; Sec. S8; SI). Altogether, experimentally measured apparent reaction orders, DFT-derived adsorption energies, and DFT-derived IR spectra show that active sites remain highly covered by either H* or HCOOH** during CO_2 hydrogenation on Cu-based catalysts. Despite the high HCOOH** coverage under conditions with high P_{CO2}, gas phase HCOOH partial pressure remains below the detection limit as predicted based on a presumed equilibrium between CO_2 + H_2 and HCOOH (Sec. S9; SI). We note that our DFT-derived adsorption energies of CO-derived surface species similarly increases with increasing H* coverage (Fig. S7; Sec. S10; SI). The saturation of surface sites by H* and HCOOH** thus also explains the observed weak CO inhibition (low coverage of CO-derived species; Fig. 2) observed in this work despite water-gas shift literature[76] previously reporting that rates on Cu(110) exhibit zeroth-order dependence on P_{CO} at $P_{CO} \approx 0.033$ bar, $P_{H2O} = 0.013$ bar, and 612 K, indicating that Cu surfaces should normally be covered by CO-derived surface species even at low CO pressures in the absence of high pressure CO_2 and H_2.

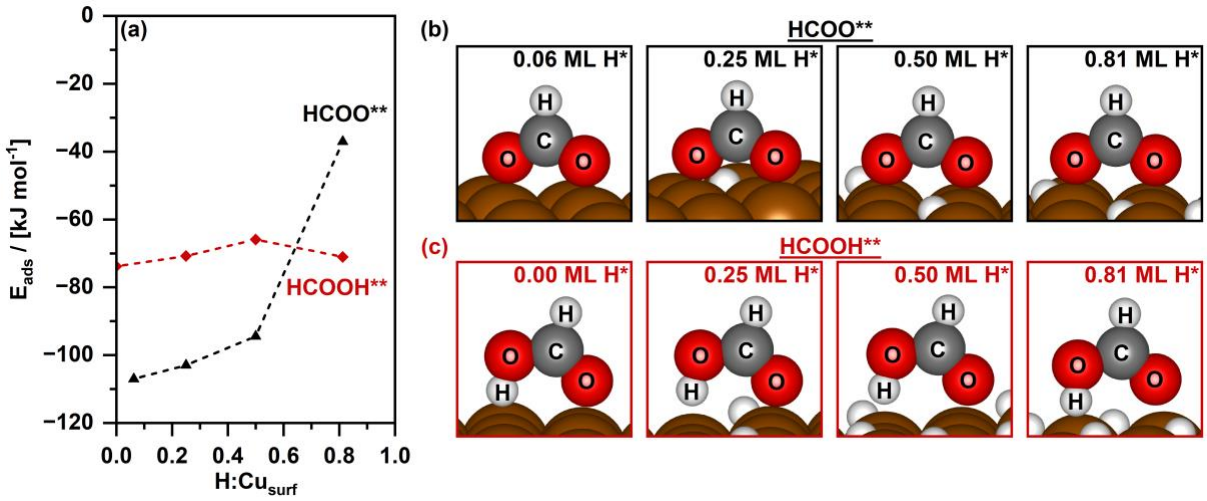

Figure 6. (a) DFT-derived electronic adsorption energies without thermal corrections (Eq. 8) of HCOO** + H* (black) and HCOOH** (red) on Cu(111) as a function of H* coverage and the predicted geometries of (b) HCOO**+H* and (c) HCOOH** with increasing H* coverage. All adsorption energies are referenced to CO_2(g) + H_2(g).

3.3. Mechanistic involvement of H_2O and CO for methanol synthesis and RWGS

Figure 7a shows that H_2O preferentially inhibits methanol synthesis rates over RWGS rates such that selectivity toward methanol decreases with increasing P_{H2O}. This is consistent with prior reports that noted more severe product inhibition for methanol synthesis than RWGS on Cu-based catalysts[77,78] and identified H_2 and H_2O as the salient species governing methanol selectivity and yield during CO_2 hydrogenation[12]. With the premise that methanol synthesis and RWGS share a common active site (Sec. 3.1), inhibition by competitive adsorption should influence both methanol synthesis and RWGS rates equally, resulting in methanol selectivity that remains invariant as in the case of CO inhibition (Fig. 2); the disparate H_2O effects for methanol synthesis and RWGS must, therefore, reflect phenomena other than competitive adsorption. That is not to say, however, that competitive adsorption by H_2O-derived species cannot exist, but simply that methanol synthesis is additionally impacted by another H_2O-driven effect. A slight decrease in RWGS rates with increasing P_{H2O} can accordingly be observed and attributed to weak competitive adsorption by H_2O (Fig. 7a).

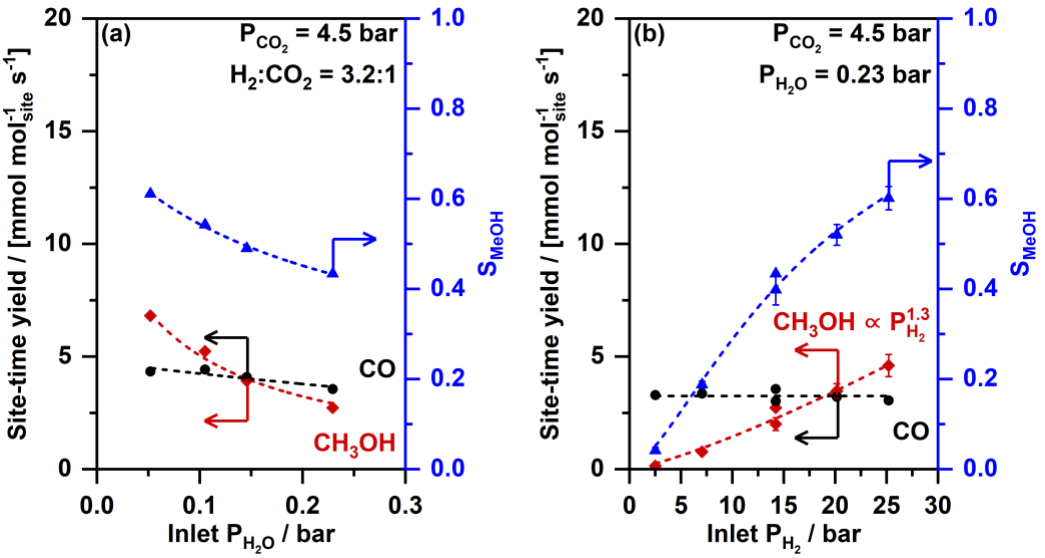

Figure 7. Methanol site-time yield (red), CO site-time yield (black), and methanol selectivity (blue) on Cu/ZnO/Al_2O_3 at 523 K as a function of (a) P_{H2O} at P_{CO2} = 4.5 bar and P_{H2} = 14.2 bar [H_2:CO_2:Ar:(He+H_2O) = 3.2:1:0.23:3.0; 2.4×10^{-4} mol s^{-1} total; X_{CO_2} = 0.0059–0.010; $Z_{ov,MeOH}$ < 0.011, $Z_{ov,RWGS}$ < 0.0055] and (b) P_{H2} under wet conditions at P_{CO2} = 4.5 bar [(He+H_2):CO_2:Ar:H_2O = 6.1:1:0.23:0.051; 2.4×10^{-4} mol s^{-1} total; X_{CO_2} = 0.0032–0.071; $Z_{ov,MeOH}$ < 0.090, $Z_{ov,RWGS}$ < 0.027]. Trendlines are shown to guide the eye. Rate and selectivity dependence on P_{H2O} on Cu/Al_2O_3 are shown in Figure S9 (Sec. S11; SI). Error bars reflect standard deviations determined from replicate GC injections.

More importantly, co-processing H_2O also increases the apparent H_2 reaction order for just the methanol synthesis reaction from 1 under dry conditions (Fig. 3) to approximately 1.3 under inlet P_{H2O} = 0.23 bar (Fig. 7b). We note that both the preferential inhibition of methanol synthesis rates and the increase in methanol synthesis H_2 reaction order by H_2O can be observed on Cu/Al_2O_3 as well (Fig. S9; Sec. S11; SI), again underscoring similarities in reaction kinetics on catalyst formulations with and without ZnO. From a mechanistic perspective, this shift in H_2 reaction order for methanol synthesis with increasing P_{H2O} indicates a change in the rate-determining step for methanol synthesis. Such changes can manifest following either a sequential or concerted H_2O formation pathway (Scheme 1). In the sequential pathway (Scheme 1a), the reactive intermediate, I_1^{**}, first forms I_2* and OH* through a reversible but not equilibrated step (step 1; Scheme 1a; k_1,

k_{-1}). OH* is then converted to H_2O* following a quasi-equilibrated step (step w; Scheme 1a; K_w), and I_2* is hydrogenated to form I_3* (step 2; Scheme 1a; k_2). In contrast, in the concerted pathway (Scheme 1b), the I_1** intermediate first interacts with H* to form a I_1/H** complex via a quasi-equilibrated step (step 0; Scheme 1b; K_0). I_1/H** then directly forms I_2* and H_2O* through a reversible but not equilibrated step without generating OH* as an intermediate (step 1; Scheme 1b; k_1, k_{-1}), and I_2* is again hydrogenated to form I_3* (step 2; Scheme 1b; k_2). Both reaction pathways involve a reversible but not equilibrated elementary step followed by an irreversible step with the intermediate (I_2*) abiding by the pseudo-steady-state hypothesis. Consequently, both reaction pathways result in rate functions with a pre-factor in addition to the functional form of Equation 22 with $K_{\text{app}} = K_{H_2O}\left(K_w K_{H_2}\right)^{-1}$ and $\varepsilon = 1$ for the sequential pathway and $K_{\text{app}} = K_{H_2O}\left(K_{H_2}\right)^{-0.5}$ and $\varepsilon = 0.5$ for the concerted pathway (derivation in Sec. S12; SI) (Eq. 23). Regardless of the mechanism for H_2O formation, the denominator of the pre-factor contains a term dependent on P_{H_2O} and P_{H_2}, causing the H_2 reaction order to change under conditions where $\frac{k_{-1}}{k_2} K_{\text{app}} \frac{P_{H_2O}}{P_{H_2}^{\varepsilon}} \gg 1$.

$$\frac{r_{\text{MeOH}}}{[L]} \propto \underbrace{\left(\frac{k_1}{1 + \frac{k_{-1}}{k_2} K_{\text{app}} \frac{P_{H_2O}}{P_{H_2}^{\varepsilon}}} \right)}_{H_2O \text{ effect}} \underbrace{\frac{4 P_{H_2}^2 P_{CO_2}}{K_{H_2} P_{H_2} \left(1 + \sqrt{1 + 8 K_I P_{CO_2}}\right)^2}}_{\text{Eq. 22}} \tag{23}$$

Scheme 1. Mechanistic motifs for water formation that lead to inhibition by H_2O that is not a consequence of competitive adsorption. H_2O formation can follow a (a) sequential pathway where OH* is formed as an intermediate or (b) a concerted pathway where OH* is not an intermediate.

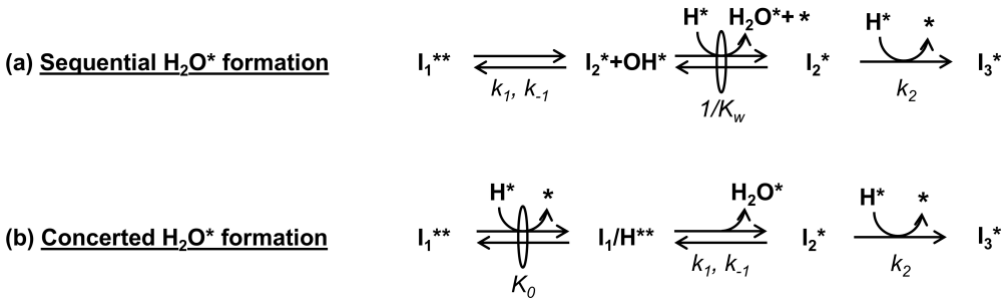

Irrespective of the mechanism for H_2O formation, the rate-determining step shifts from step 1 (k_1, k_{-1}) in the limit of $P_{H2O} = 0$ (Eq. 24a) to step 2 (k_2) in the limit of infinite P_{H2O} (Eq. 24b) as step 1 approaches equilibrium.

$$\lim_{P_{H_2O}\to 0} \frac{r}{[L]} \propto k_1 \tag{24a}$$

$$\lim_{P_{H_2O}\to \infty} \frac{r}{[L]} \propto k_2 \left(\frac{k_1}{k_{-1}}\right) \frac{P_{H_2}^{1+\varepsilon}}{K_{\text{app}} P_{H_2O}} \tag{24b}$$

The distinguishing feature between the two pathways thus lies in the value of ε, where the sequential pathway is associated with $\varepsilon = 1$ such that the H_2 reaction order will shift from 1 to 2 with increasing P_{H2O} and the concerted pathway is instead associated with $\varepsilon = 0.5$ such that the H_2 reaction order will shift from 1 to 1.5 with increasing P_{H2O} (derivation in Sec. S12; SI). While ε can be estimated based on apparent H_2 reaction orders under H_2O co-feed (Fig. 7b), it is often unclear *a priori* whether the P_{H2O} applied is sufficiently high to accurately identify the maximum H_2 reaction order. Instead, Equation 24b can be leveraged to evaluate ε based on the ratio in rates at distinct P_{H2} with increasing P_{H2O} (Eq. 25) as shown in Figure 8.

$$\lim_{P_{H_2O}\to\infty} \frac{r|_{P_{H_2}=P_1}}{r|_{P_{H_2}=P_2}} = \left(\frac{P_1}{P_2}\right)^{1+\varepsilon} \Rightarrow 1+\varepsilon = \lim_{P_{H_2O}\to\infty} \frac{\ln\left(\frac{r|_{P_{H_2}=P_1}}{r|_{P_{H_2}=P_2}}\right)}{\ln\left(\frac{P_1}{P_2}\right)} \quad (25)$$

For methanol synthesis at P_{H2} = 24.2 bar (P_1) and 4.7 bar (P_2), ε asymptotically approaches 0.5 with increasing P_{H2O}, showing that a feature akin to Scheme 1b is consistent with the observed reaction kinetics for methanol synthesis. On the other hand, ε is expectedly 0 for RWGS, again indicating disparate dependence on H_2O pressure for methanol synthesis and RWGS.

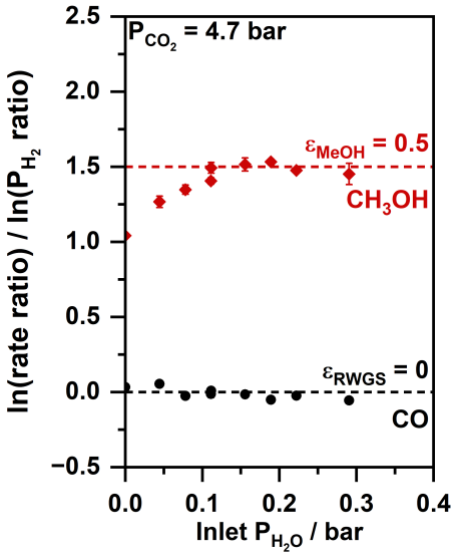

Figure 8. Ratio in methanol (red) and CO (black) site-time yields between P_{H2} = 24.2 bar and 4.7 bar divided by ratio in P_{H2} as defined in Equation 25 on $Cu/ZnO/Al_2O_3$ at 523 K as a function of P_{H2O} at P_{CO2} = 4.7 bar [H_2:CO_2:Ar:(He+H_2O) = 1.0:1:0.23:4.4 or 5.1:1:0.23:0.24; 2.1×10^{-4} mol s^{-1} total; X_{CO_2} = 0.0039–0.028; $Z_{ov,MeOH}$ < 0.080, $Z_{ov,RWGS}$ < 0.020]. Trendlines are shown to guide the eye. Error bars reflect standard deviations determined from replicate GC injections.

Per our discussion at the start of this section, while H_2O preferentially inhibits methanol synthesis rates via the mechanistic motif shown in Scheme 1b, H_2O can still exhibit weak competitive adsorption evidenced by the small decrease in RWGS rates with increasing P_{H2O}. This competitive adsorption would normally inhibit methanol synthesis and RWGS rates equally as they share a common active site, but its effect on methanol synthesis is shadowed by the contribution from the change in rate-determining step, resulting in distinct ε values for methanol

synthesis and RWGS (Fig. 8). Accordingly, the functional form of Equation 22 and the invariant H_2 reaction order for RWGS with increasing P_{H2O} (Figs. 7b and 8) together demonstrate that competitive adsorption by the H_2O-derived surface species should yield an additional term in the site balance (Eq. 17) that also exhibits a $\sqrt{P_{H_2}}$ dependence such that P_{H2} can still factor out in the denominator of Equation 22 and the apparent H_2 reaction order for RWGS remains invariant with increasing P_{H2O}. In other words, if the H_2O-derived surface species resulted in just a P_{H2O} term in the site balance (e.g., H_2O^* is the most abundant H_2O-derived intermediate), P_{H2} will no longer factor out as in Equation 22, and H_2 reaction order for RWGS will change with increasing P_{H2O}, which is inconsistent with the data reported in Figure 8. Inhibition by competitive adsorption of CO (Fig. 2) similarly does not change the H_2 reaction orders for methanol synthesis as CO inhibition effects measured at P_{H2} from 4.7 bar to 23.4 bar are comparable (Sec. S13; SI), indicating that competitive adsorption by the CO-derived surface species must also exhibit a $\sqrt{P_{H_2}}$ dependence in the site balance (Eqs. 17 and 22). In sum, these observations show that H_2O predominantly forms hydronium-type surface species ($H_2O^* + H^* \rightleftarrows H_2O/H^* + *$) and CO predominantly forms HCO/COH-type surface species ($CO^* + H^* \rightleftarrows HCO^*$ (or COH^*) $+ *$) upon adsorption, analogous to how CO_2 predominantly forms HCOOH** upon adsorption. The formation of these H_2O- and CO-derived surface species is not surprising given the favorable adsorption energies derived from DFT (Sec. S14; SI) and the fact that HCO/COH-type species serve as the first partially hydrogenated intermediate commonly proposed during CO hydrogenation[18,79]. As the DFT-derived adsorption energy for HCO* is lower than that for COH* on Cu(111) (Sec. S14; SI), we will henceforth assign HCO* as the CO-derived surface species.

The presence of H_2O/H* and HCO* over their non-hydrogenated counterparts (H_2O* and CO*) can again be attributed to the high H* coverage under methanol synthesis conditions. In essence, the high P_{H2} applied leads to an H*-saturated surface. CO_2*, CO*, and H_2O* formed either from adsorption of gas-phase species or from reaction are each then hydrogenated and in equilibrium with HCOOH**, HCO*, and H_2O/H*, respectively, such that coverages of CO_2*, CO*, and H_2O* remain low and negligible (Scheme 2). Contributions of HCOOH**, HCO*, H_2O/H*, and H* to the site balance each exhibit a $\sqrt{P_{H_2}}$ dependence per site, leading to H_2 reaction orders that are invariant with competitive adsorption. Beyond these adsorption phenomena is the change in the rate-determining step of methanol synthesis with increasing P_{H2O} that ultimately results in more significant H_2O inhibition along with a change in H_2 reaction order for just the methanol synthesis reaction. Altogether, the functional forms of the rate expressions for methanol synthesis and RWGS are:

$$\frac{r_{\mathrm{MeOH}}}{[L]} = \frac{\left(\frac{k_{\mathrm{app,MeOH}}}{1+\frac{k_{-1}}{k_2}K_{\mathrm{app}}\frac{P_{H_2O}}{P_{H_2}^{0.5}}}\right)P_{H_2}^2 P_{CO_2}}{K_{H_2}P_{H_2}\left\{1+\underbrace{K_{HCO}P_{CO}+K_{H_2O/H}P_{H_2O}}_{\text{typically small}}+\left[\left(1+\underbrace{K_{HCO}P_{CO}+K_{H_2O/H}P_{H_2O}}_{\text{typically small}}\right)^2+8K_IP_{CO_2}\right]^{1/2}\right\}^2} \quad (26a)$$

$$\frac{r_{\mathrm{RWGS}}}{[L]} = \frac{k_{\mathrm{app,RWGS}}P_{H_2}P_{CO_2}}{K_{H_2}P_{H_2}\left\{1+\underbrace{K_{HCO}P_{CO}+K_{H_2O/H}P_{H_2O}}_{\text{typically small}}+\left[\left(1+\underbrace{K_{HCO}P_{CO}+K_{H_2O/H}P_{H_2O}}_{\text{typically small}}\right)^2+8K_IP_{CO_2}\right]^{1/2}\right\}^2} \quad (26b)$$

where K_I, K_{HCO} and $K_{H_2O/H}$ are equilibrium constants for the formation of HCOOH**, HCO*, and H_2O/H* from CO_2(g)+2H*, CO(g)+H*, and H_2O(g)+H*, respectively. Terms associated with HCO* and H_2O/H* appear twice in the denominator due to a mathematical artifact associated with

the simultaneous presence of surface intermediates that occupy one site and surface intermediates (HCOOH**) that occupy two sites. The coverages of CO- and H_2O-derived surface intermediates are likely low under the conditions employed since rates do not decrease significantly with increasing P_{CO} and P_{H2O} except for methanol synthesis under H_2O co-feed, thereby limiting the ability to pinpoint effects (e.g., changes in H_2 reaction orders) associated with these species. We note, however, that further increases in P_{H2O} could lead to catalyst deactivation[57] and further increases in P_{CO} could convolute thermodynamic and kinetic driving forces of RWGS and confound the source of methanol. Thus, the conclusion presented above, while potentially subject to limitations, is nonetheless consistent with all our kinetic data. In the following section, we leverage KIE to further demonstrate the provenance of a shift in rate-determining step for methanol synthesis with increasing P_{H2O} under methanol synthesis conditions.

Scheme 2. Interaction of gaseous CO_2, CO, and H_2O with the H*-saturated surface.

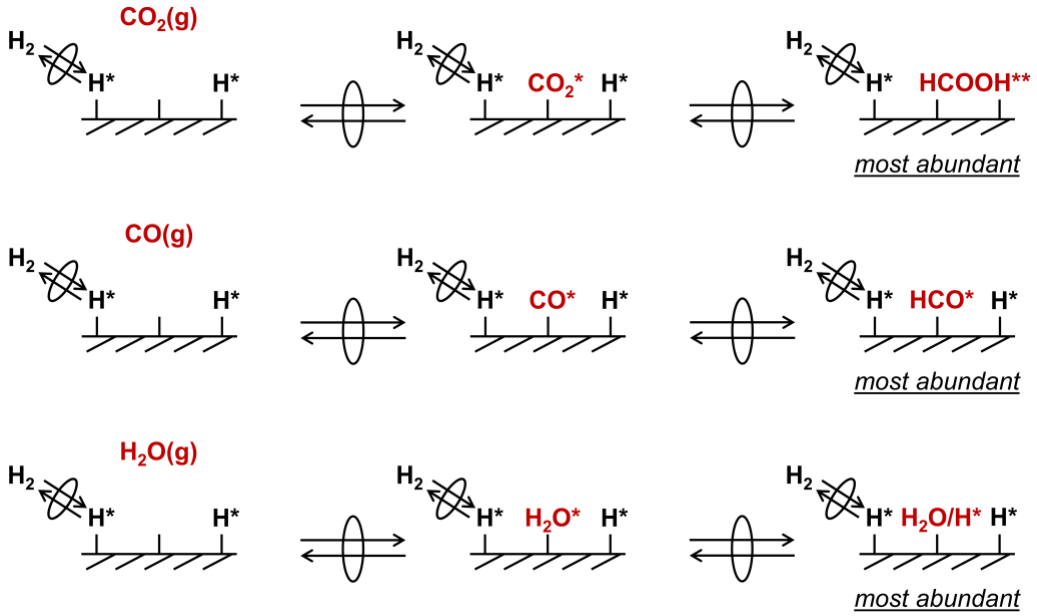

3.4. Kinetic isotope effect under dry and wet conditions

Figure 9a shows that, under a H_2O-free feed, methanol synthesis exhibits an inverse H_2/D_2 KIE while RWGS exhibits a negligible KIE, in agreement with earlier work by Kunkes et al.[24]. These measured KIEs, the disparate H_2O effects discussed in the previous section, and reversibility-based arguments[12] all point to methanol synthesis and RWGS undergoing a branching reaction network with distinct intermediates and pathways. Beyond comparisons between the two reactions, however, decreasing KIE (larger difference between rates from CO_2+H_2 and rates from CO_2+D_2) with increasing $P_{H2O/D2O}$ for methanol synthesis further demonstrates a shift in rate-determining step under wet conditions (Fig. 9b). We surmise that this change in KIE may have also contributed to the change in KIE with increasing reaction temperature and conversion (i.e., increasing P_{H2O}) as observed by Kunkes et al.[24]. Furthermore, the KIE for RWGS is expectedly invariant with increasing $P_{H2O/D2O}$, commensurate with the above observation that H_2O does not alter the rate-determining step for RWGS. In the following section, we consolidate all our experimental, theoretical, and mathematical evidence into one comprehensive reaction mechanism for CO_2 hydrogenation on Cu-based catalysts.

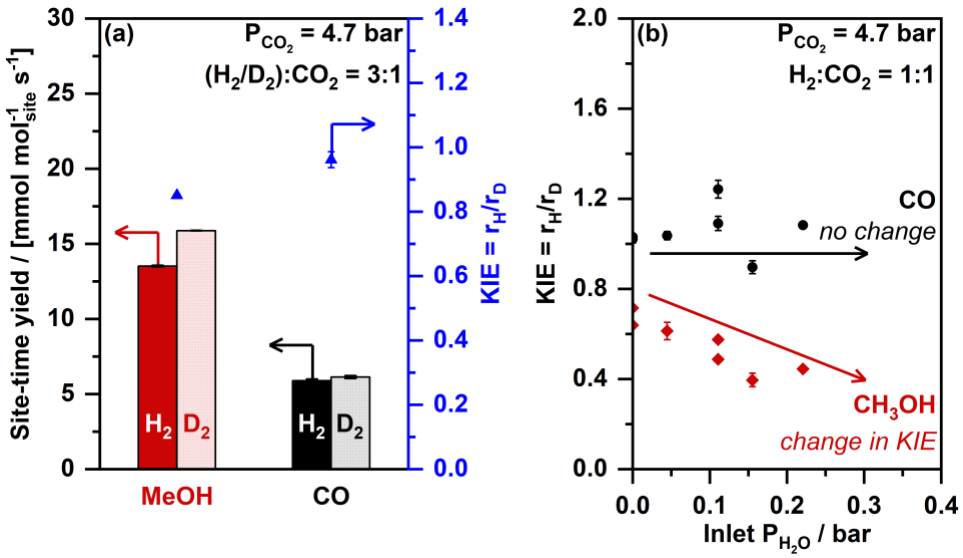

Figure 9. (a) Methanol (red) and CO (black) site-time yields on $Cu/ZnO/Al_2O_3$ at 523 K when H_2 or D_2 is used at P_{CO2} = 4.7 bar [$(H_2/D_2):CO_2$:(Ar+He) = 3:1:2.8; 1.5×10^{-4} mol s^{-1} total; X_{CO_2} = 0.012–0.014; $Z_{ov,MeOH}$ < 0.011, $Z_{ov,RWGS}$ < 0.0017]. The kinetic isotopic effects for methanol synthesis and RWGS are shown in blue on the secondary axis. (b) Kinetic isotopic effect of methanol synthesis (red) and RWGS (black) on $Cu/ZnO/Al_2O_3$ as a function of P_{H2O} at P_{CO2} = 4.7 bar [$(H_2/D_2):CO_2$:Ar:(He+H_2O/D_2O) = 1:1:0.33:(4.4–4.5); 1.5×10^{-4}–2.1×10^{-4} mol s^{-1} total; X_{CO_2} = 0.0039–0.011; $Z_{ov,MeOH}$ < 0.12, $Z_{ov,RWGS}$ < 0.017]. Trendlines are shown to guide the eye. Error bars reflect standard deviations determined from replicate GC injections.

3.5. Reaction mechanism and microkinetic modeling

Sections 3.1 to 3.4, in sum, show that: (i) methanol synthesis and RWGS share a common active site, (ii) the catalyst surface is highly covered by H* and HCOOH** under methanol synthesis conditions while HCO* and H_2O/H* species are present at low coverages when co-processing CO and H_2O (Eq. 26), (iii) the disparate rate-determining steps for methanol synthesis and RWGS involve intermediates totaling to four and two H-atoms, respectively, under dry conditions, and (iv) methanol synthesis exhibits two rate-determining steps that are P_{H2O}-dependent (and, consequently, H_2O* and H_2O/H* coverage-dependent) akin to Scheme 1b such that H_2O preferentially inhibits methanol synthesis rates and increases H_2 apparent reaction order

(Eq. 24). Scheme 3 illustrates the reaction mechanism for CO_2 hydrogenation congruent with the above critical inferences.

Scheme 3. Branching reaction mechanism for CO_2 hydrogenation congruent with experimental and theoretical observations. Quasi-equilibrated elementary steps are shown with reversible arrows with an oval, and the MASIs (HCOOH** and H*) are shown in bold.

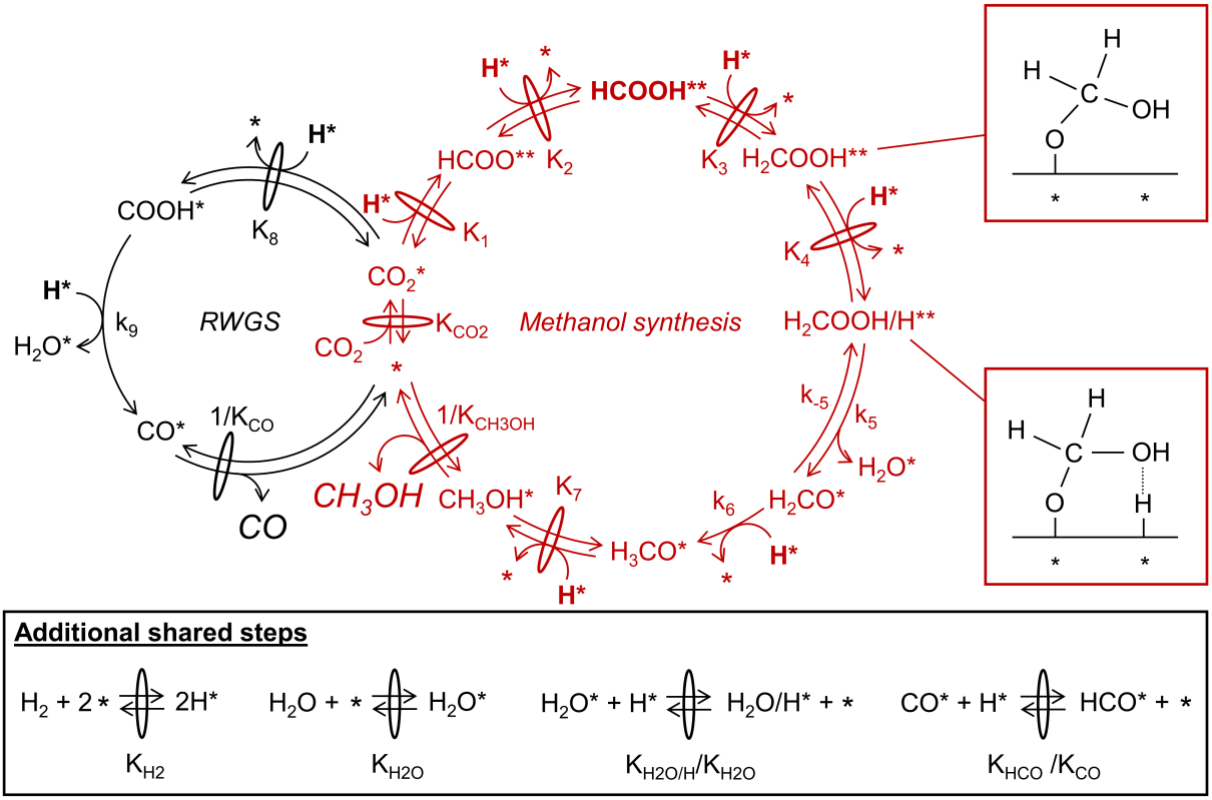

In detail, methanol synthesis occurs first via sequential and equilibrated hydrogenation of CO_2* to HCOO**, HCOOH**, H_2COOH**, and, lastly, the H_2COOH/H** complex. Monodentate formate (HCOO*) and bidentate formate (HCOO**) are likely in equilibrium; the formation of HCOOH** (MASI) through either HCOO* or HCOO** (Scheme 4), accordingly, are kinetically equivalent. Scheme 3 hence only shows the HCOO** pathway for consistency with experimental infrared spectra[35,36,66]. The H_2COOH/H** intermediate (four H-atoms in accordance with (iii)) then undergoes a reversible but not necessarily equilibrated C–O cleavage to form H_2O* and a surface formyl (H_2CO*), which is subsequently hydrogenated to a surface

methoxy. These two steps together serve as the mechanistic motif akin to Scheme 1b to capture the effect of H_2O on methanol synthesis (point (iv)). Finally, the surface methoxy is hydrogenated and desorbs reversibly, yielding methanol and completing the methanol synthesis catalytic cycle.

Scheme 4. Quasi-equilibrated and kinetically equivalent bidentate formate and monodentate formate pathways for the formation of molecular formic acid.

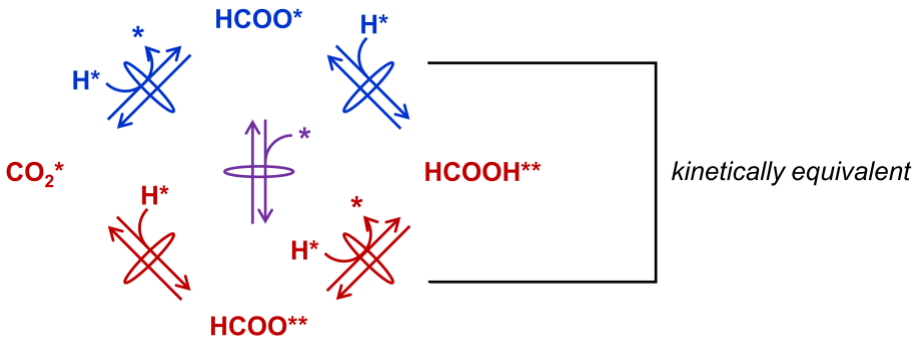

The RWGS catalytic cycle proceeds down the carboxylate pathway rather than the formate pathway, consistent with the disparate H_2O effects and KIEs for methanol synthesis and RWGS (Sec. 3.3–3.4) and with reported DFT calculations[18,80]. CO_2* first forms a surface carboxylate (COOH*) via an equilibrated hydrogenation step. COOH* then undergoes rate-determining H*-assisted C–OH cleavage to yield H_2O* and CO*, reflecting the requirement for the rate-determining step of RWGS to involve intermediates totaling to two H-atoms (point (iii)). CO* is then in equilibrium with HCO* but must ultimately desorb reversibly as CO(g) to complete the RWGS catalytic cycle. The lack of two rate-determining steps in the carboxylate cycle reflects the absence of any effect of water concentration on the apparent H_2 reaction order and KIE for RWGS. Furthermore, the proposed carboxylate pathway for CO formation does not require the formation of C–H bond(s) from CO_2 followed by subsequent C–H bond cleavage step(s) to yield CO, a feature otherwise necessary for formates to be involved in the RWGS catalytic cycle.

Knowledge of the constitutive elementary steps now enables derivation of closed-form rate expressions for both methanol synthesis (Eq. 27) and RWGS (Eq. 28) using the quasi-equilibrium approximation and the pseudo-steady-state hypothesis wherever appropriate (full derivation shown in Sec. S15; SI):

$$\frac{\vec{r}_{\mathrm{MeOH}}}{[L]} = \frac{\alpha P_{CO_2} P_{H_2}}{\left(1 + \beta \frac{P_{H_2O}}{\sqrt{P_{H_2}}}\right)\left[1 + \zeta P_{CO} + \kappa P_{H_2O} + \sqrt{\left(1 + \zeta P_{CO} + \kappa P_{H_2O}\right)^2 + \lambda P_{CO_2}}\right]^2} \tag{27}$$

$$\frac{\vec{r}_{\mathrm{RWGS}}}{[L]} = \frac{\omega P_{CO_2}}{\left[1 + \zeta P_{CO} + \kappa P_{H_2O} + \sqrt{\left(1 + \zeta P_{CO} + \kappa P_{H_2O}\right)^2 + \lambda P_{CO_2}}\right]^2} \tag{28}$$

where $\alpha = 4k_5K_1K_2K_3K_4K_{CO_2}K_{H_2}$, $\beta = k_{-5}K_{H_2O}\left(k_6\sqrt{K_{H_2}}\right)^{-1}$, $\zeta = K_{HCO}$, $\kappa = K_{H_2O/H}$, $\lambda = 8K_1K_2K_{CO_2}$, and $\omega = 4k_9K_8K_{CO_2}$ with all rate and equilibrium constants defined in Scheme 3. These rate expressions are expectedly in agreement with Equation 26, which was postulated based on empirical trends. We note, however, that Scheme 3 considers one irreversible elementary step for each catalytic cycle despite the reversible nature of CO_2 hydrogenation. Accordingly, the derived rate expressions are strictly the forward rates (irreversible) rather than the net rates (reversible). While reported rates herein are predominantly measured under irreversible conditions where the overall and effective reversibility values are far below unity, these forward rate expressions must be converted to net rate expressions via reversibility formalisms (Eq. 29) to capture any potential thermodynamic contributions to observed net rates. Specific to this case, Equation 29 utilized the equality $Z_{\mathrm{eff}} = Z_{\mathrm{ov}}$ as all elementary steps have unity stoichiometric number (i.e., stoichiometrically regular)[81], where Z_{ov} is as defined in Equation 6 (Sec. 2.1).

$$r = \vec{r} - \overleftarrow{r} = \vec{r}(1 - Z_{\mathrm{eff}}) = \vec{r}\left(1 - Z_{\mathrm{ov}}^{1/\bar{\sigma}}\right) = \vec{r}\left(1 - Z_{\mathrm{ov}}^{1/1}\right) \tag{29}$$

Parameter estimation was performed using the integral model of plug flow reactors (Eq. 30), Bayesian statistics, and a comprehensive experimental dataset measuring (i) H_2 effect at P_{CO2} = 0.25, 0.5, and 4.7 bar, (ii) CO_2 effect at P_{H2} = 0.75, 14.1, and 23.4 bar, (iii) H_2O effect at (P_{CO2}, P_{H2}) = (4.7 bar, 4.7 bar), (4.5 bar, 14.2 bar), and (4.7 bar, 24.2 bar), (iv) H_2 effect at P_{CO2} = 4.5 bar and P_{H2O} = 0.23 bar, (v) CO effect at P_{CO2} = 4.7 bar and P_{H2} = 23.4 bar, and (vi) space velocity effect[12] at P_{CO2} = 4.7 bar and P_{H2} = 4.7, 8.9, 14.0, and 23.4 bar.

$$\frac{dF_i}{dn_{\text{site}}} = \nu_{i,\text{MeOH}} \frac{r_{\text{MeOH}}}{[L]} + \nu_{i,\text{RWGS}} \frac{r_{\text{RWGS}}}{[L]} \tag{30a}$$

$$F_{i,\text{out}} - F_{i,\text{in}} = \int_0^{n_{\text{site}}} \left(\nu_{i,\text{MeOH}} \frac{r_{\text{MeOH}}}{[L]} + \nu_{i,\text{RWGS}} \frac{r_{\text{RWGS}}}{[L]} \right) dn \tag{30b}$$

$$P_i = \frac{F_i}{\sum_j F_j} P_{\text{tot}} \tag{30c}$$

In all cases, predicted methanol and CO site-time yields using Equations 27 to 30 accurately reflect observed reaction orders, rates, and, therefore, selectivity as shown in Figures 10 to 15 for the six datasets listed above, underscoring the validity of the proposed single-site, high-coverage reaction mechanism in describing both methanol synthesis and RWGS. Section S16 (SI) lists the fitted parameters along with their 95% highest posterior density (HPD) intervals, illustrates the overall parity plot (Fig. S13; SI), and details the sensitivity analysis for predicted effluent methanol and CO flow rates for $Cu/ZnO/Al_2O_3$. Microkinetic modeling for Cu/Al_2O_3 is then presented in Section S17 (SI).

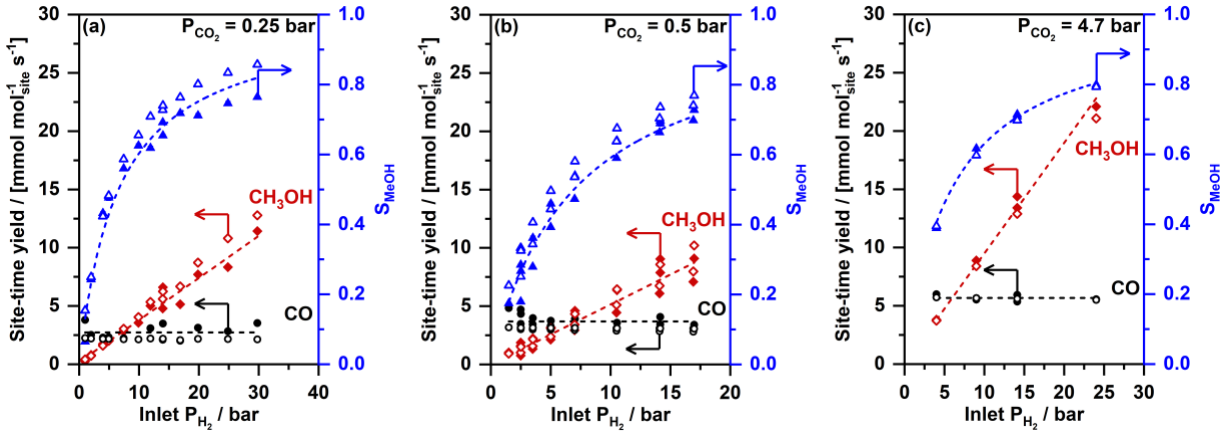

Figure 10. Observed (filled symbol) and predicted (open symbol) methanol site-time yield (red), CO site-time yield (black), and methanol selectivity (blue) on Cu/ZnO/Al_2O_3 at 523 K as a function of P_{H2} at (a) P_{CO2} = 0.25 bar [(He+Ar+H_2):CO_2 = (80.4–131.9):1; 1.5×10^{-4}–4.2×10^{-4} mol s^{-1} total; X_{CO_2} = 0.016–0.10; $Z_{ov,MeOH} < 0.58$, $Z_{ov,RWGS} < 0.015$], (b) P_{CO2} = 0.5 bar [(He+H_2):CO_2:Ar = 6.8:1:0.24 or 37.8:1:1.2; 3.0×10^{-4} mol s^{-1} total; X_{CO_2} = 0.012–0.096; $Z_{ov,MeOH} < 0.47$, $Z_{ov,RWGS} < 0.028$], and (c) P_{CO2} = 4.7 bar [(He+H_2):CO_2:Ar = 5.4:1:0.21; 2.9×10^{-4} mol s^{-1} total; X_{CO_2} = 0.0067–0.019; $Z_{ov,MeOH} < 0.058$, $Z_{ov,RWGS} < 0.0030$]. Trendlines are shown to guide the eye. Error bars reflect standard deviations determined from replicate GC injections.

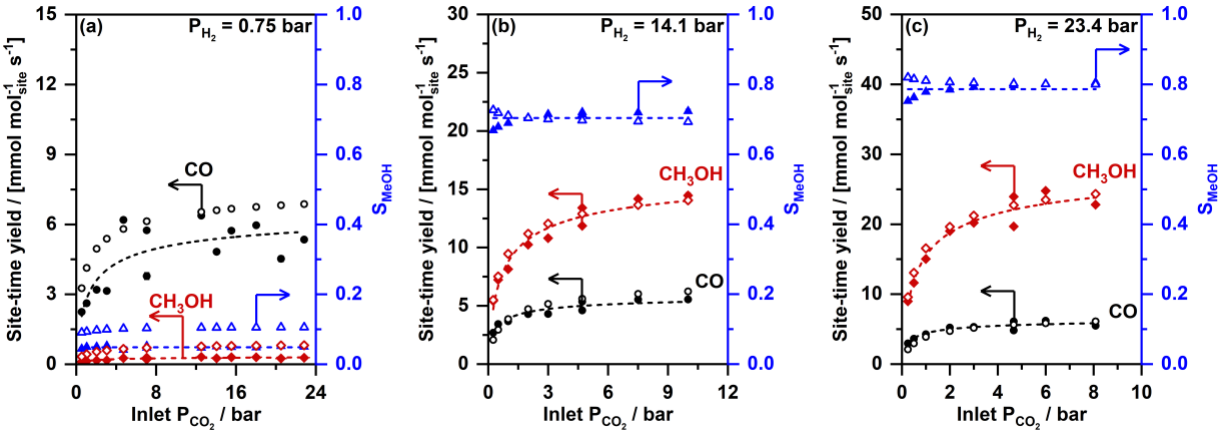

Figure 11. Observed (filled symbol) and predicted (open symbol) methanol site-time yield (red), CO site-time yield (black), and methanol selectivity (blue) on Cu/ZnO/Al_2O_3 at 523 K as a function of P_{CO2} at (a) P_{H2} = 0.75 bar [H_2:(He+CO_2):Ar = 1:24.2:10.6 or 1:31.3:3.6; 3.8×10^{-4} mol s^{-1} total; X_{CO_2} = 0.00043–0.0079; $Z_{ov,MeOH} < 0.16$, $Z_{ov,RWGS} < 0.0040$], (b) P_{H2} = 14.1 bar [H_2:(He+CO_2):Ar = 1:1.1:0.07; 2.9×10^{-4} mol s^{-1} total; X_{CO_2} = 0.0066–0.090; $Z_{ov,MeOH} < 0.026$, $Z_{ov,RWGS} < 0.0055$], and (c) P_{H2} = 23.4 bar [H_2:(He+CO_2):Ar = 1:0.35:0.11; 3.1×10^{-4} mol s^{-1} total; X_{CO_2} = 0.0070–0.081; $Z_{ov,MeOH} < 0.0055$, $Z_{ov,RWGS} < 0.0021$]. Trendlines are shown to guide the eye. Error bars reflect standard deviations determined from replicate GC injections.

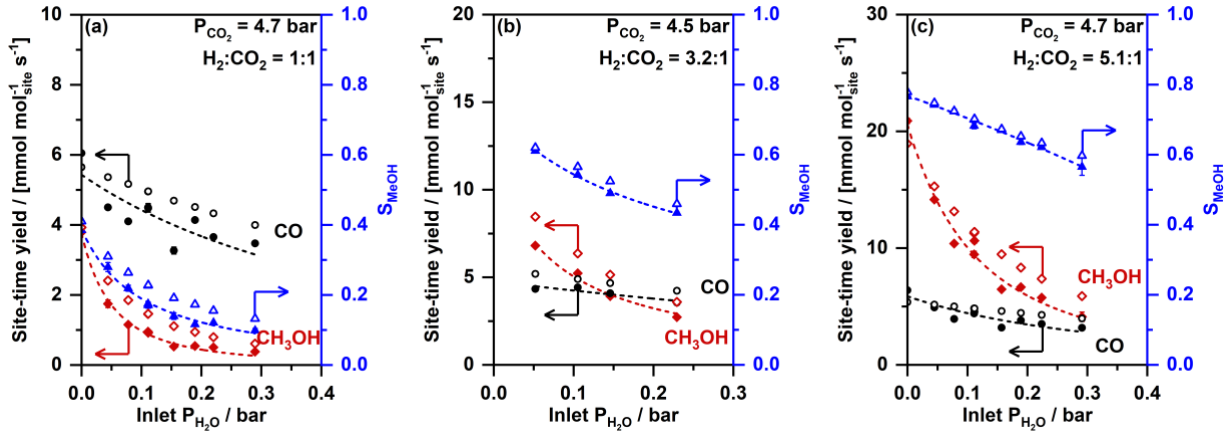

Figure 12. Observed (filled symbol) and predicted (open symbol) methanol site-time yield (red), CO site-time yield (black), and methanol selectivity (blue) on Cu/ZnO/Al_2O_3 at 523 K as a function of P_{H2O} at (a) P_{CO2} = 4.7 bar and H_2:CO_2 = 1:1 [H_2:CO_2:Ar:(He+H_2O) = 1:1:0.23:4.4; 2.1×10^{-4} mol s^{-1} total; X_{CO_2} = 0.0039–0.010; $Z_{ov,MeOH} < 0.080$, $Z_{ov,RWGS} < 0.020$], (b) P_{CO2} = 4.5 bar and H_2:CO_2 = 3.2:1 [H_2:CO_2:Ar:(He+H_2O) = 3.2:1:0.23:3.0; 2.4×10^{-4} mol s^{-1} total; X_{CO_2} = 0.0059–0.010; $Z_{ov,MeOH} < 0.011$, $Z_{ov,RWGS} < 0.0055$], and (c) P_{CO2} = 4.7 bar and H_2:CO_2 = 5.1:1 [H_2:CO_2:Ar:(He+H_2O) = 5.1:1:0.23:0.24; 2.1×10^{-4} mol s^{-1} total; X_{CO_2} = 0.0073–0.028; $Z_{ov,MeOH} <$ 0.0089, $Z_{ov,RWGS} < 0.0037$]. Trendlines are shown to guide the eye. Error bars reflect standard deviations determined from replicate GC injections.

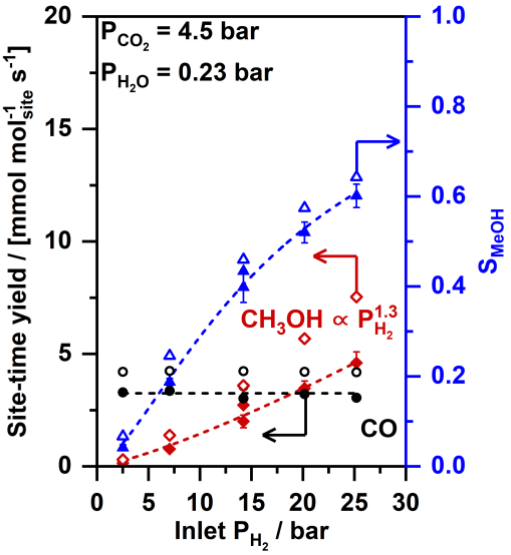

Figure 13. Observed (filled symbol) and predicted (open symbol) methanol site-time yield (red), CO site-time yield (black), and methanol selectivity (blue) on Cu/ZnO/Al_2O_3 at 523 K as a function of P_{H2} under wet conditions at P_{CO2} = 4.5 bar [(He+H_2):CO_2:Ar:H_2O = 6.1:1:0.23:0.051; 2.4×10^{-4} mol s^{-1} total; X_{CO_2} = 0.0032–0.071; $Z_{ov,MeOH} < 0.090$, $Z_{ov,RWGS} < 0.027$]. Trendlines are shown to guide the eye. Error bars reflect standard deviations determined from replicate GC injections.

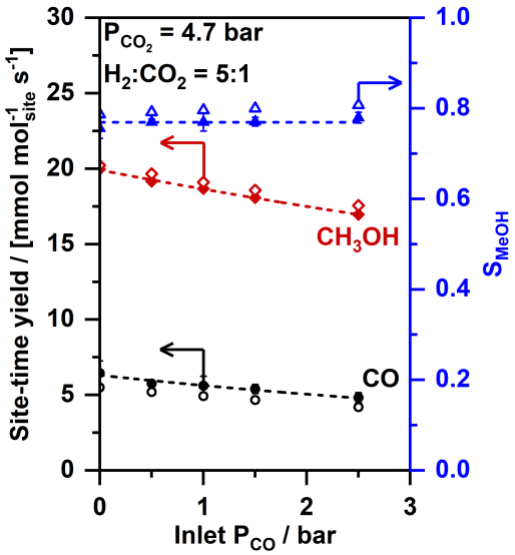

Figure 14. Observed (filled symbol) and predicted (open symbol) methanol site-time yield (red), CO site-time yield (black), and methanol selectivity (blue) on Cu/ZnO/Al_2O_3 at 523 K as a function of P_{CO} at P_{CO2} = 4.7 bar [H_2:CO_2:Ar:(He+CO) = 5:1:0.45:2.3; 2.5×10^{-4} mol s^{-1} total; X_{CO_2} = 0.015–0.019; $Z_{\mathrm{ov,MeOH}}$ < 0.0045, $Z_{\mathrm{ov,RWGS}}$ < 0.15]. CO site-time yield during CO co-feed were determined by subtracting methanol site-time yield from H_2O site-time yield. Trendlines are shown to guide the eye. Error bars reflect standard deviations determined from replicate GC injections.

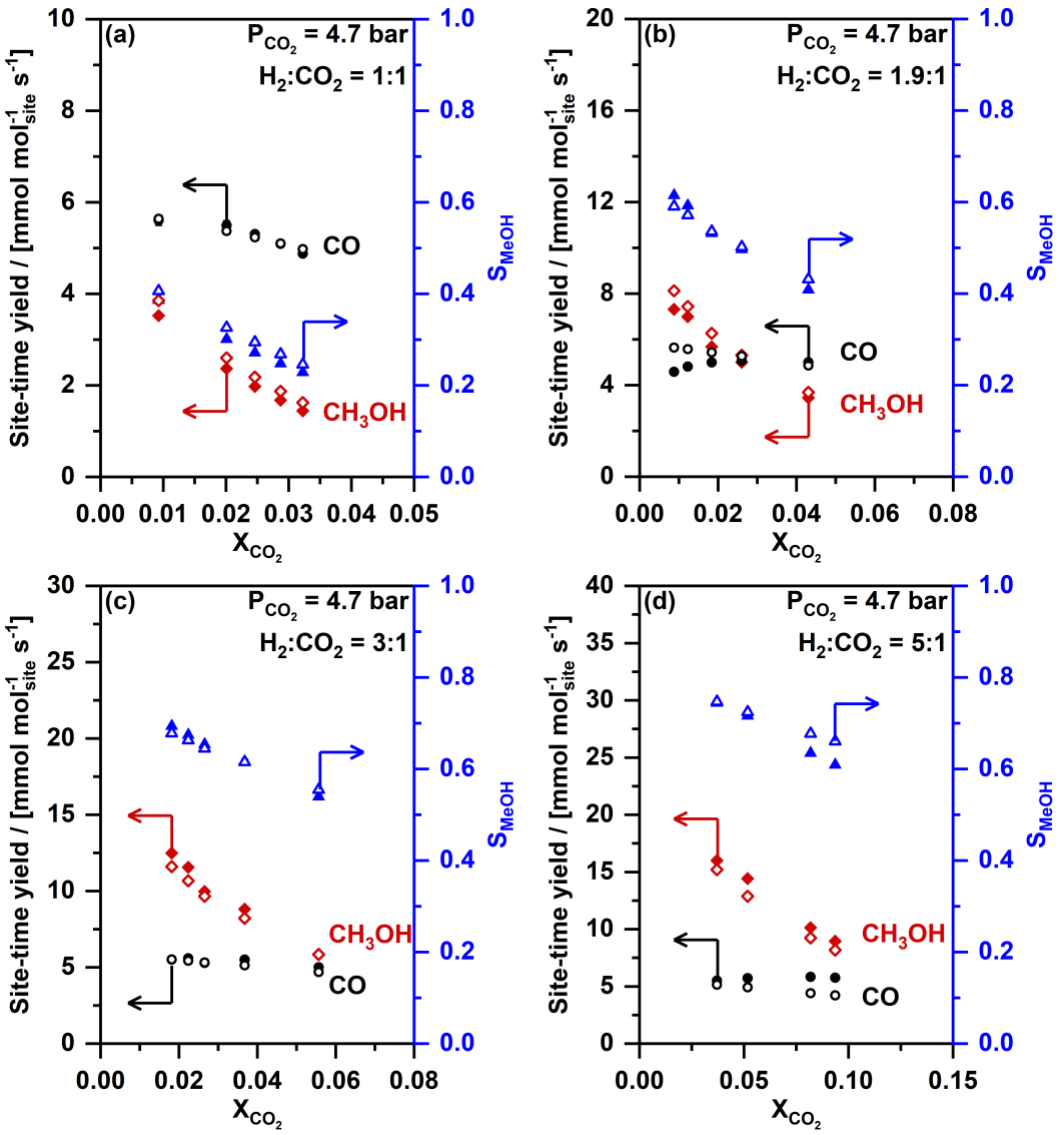

Figure 15. Observed (filled symbol) and predicted (open symbol) methanol site-time yield (red), CO site-time yield (black), and methanol selectivity (blue) on Cu/ZnO/Al_2O_3 at 523 K as a function of X_{CO_2} at P_{CO2} = 4.7 and H_2:CO_2 = (a) 1:1 [H_2:CO_2:Ar = 1:1:2.4; 6.9×10^{-5}–3.5×10^{-4} mol s^{-1} total; X_{CO_2} = 0.0093–0.032; $Z_{ov,MeOH}$ < 0.60, $Z_{ov,RWGS}$ < 0.084], (b) 1.9:1 [H_2:CO_2:Ar = 1.9:1:1.5; 6.9×10^{-5}–4.8×10^{-4} mol s^{-1} total; X_{CO_2} = 0.0088–0.043; $Z_{ov,MeOH}$ < 0.31, $Z_{ov,RWGS}$ < 0.068], (c) 3:1 [H_2:CO_2:Ar = 3:1:(0.39–2.5); 1.0×10^{-4}–3.6×10^{-4} mol s^{-1} total; X_{CO_2} = 0.018–0.056; $Z_{ov,MeOH}$ < 0.22, $Z_{ov,RWGS}$ < 0.065], and (d) 5:1 [H_2:CO_2:Ar = 5:1:0.86; 8.7×10^{-5}–3.3×10^{-4} mol s^{-1} total; X_{CO_2} = 0.037–0.094; $Z_{ov,MeOH}$ < 0.11, $Z_{ov,RWGS}$ < 0.074]. Error bars reflect standard deviations determined from replicate GC injections.

From a theoretical perspective, DFT-derived electronic energies of intermediates and transition states involved in steps 4 to 6 of the methanol synthesis pathway (Scheme 3) are shown

in Figure 16 with all energies referenced to H_2COOH^{**}, the reactant for step 4. Formation of the H_2COOH/H^{**} complex from infinitely separated H_2COOH^{**} and H^* is only slightly endothermic (ΔE = +3 kJ mol^{-1}) (step 4; Scheme 3). This H_2COOH/H^{**} complex undergoes concerted C–O bond dissociation and H_2O formation with an activation energy of 137 kJ mol^{-1} ($\ddagger_5$; Fig. 16a) to yield H_2CO^* and H_2O^* (step 5; Scheme 3; akin to Scheme 1b). H_2CO^* is subsequently hydrogenated to H_3CO^* with an activation barrier of 36 kJ mol^{-1} (step 6; Scheme 3). The high activation barrier of step 5 is congruent with the mechanistic picture that step 5 is the rate-determining step under dry reaction conditions; step 6 only becomes rate-determining when step 5 is equilibrated under conditions with sufficiently high P_{H2O}. Predicted energies for the sequential H_2O formation pathway, where H_2COOH^{**} first undergoes C–O bond dissociation ($\ddagger_{5A}$; Fig. 16b; E_A = 61 kJ mol^{-1}) to form H_2CO^* and OH^* followed by OH^* hydrogenation to H_2O^* ($\ddagger_{5B}$; Fig. 16c; E_A = 104 kJ mol^{-1}), further corroborate the mechanistic picture shown in Scheme 3 as the concerted H_2O^* formation pathway from $H_2COOH^*+H^*$ (Scheme 1b) indeed leads to an overall lower energy route in comparison to the sequential H_2O^* formation pathway (Scheme 1a), with the transition state for the concerted pathway ($\ddagger_5$) being 28 kJ mol^{-1} lower in energy than the transition state of the OH^* hydrogenation step in the sequential pathway ($\ddagger_{5B}$).

DFT-derived free energies of intermediates and transition states are then used to predict H_2/D_2 KIEs for methanol synthesis based on Scheme 3 (details in Sec. S18; SI). These results show a decrease in DFT-derived KIE (1.43 and 0.71 under dry and wet conditions, respectively) as the rate-determining step shifts from step 5 to step 6 (Scheme 3), consistent with experimental observations (0.7 and 0.4 under dry and wet conditions, respectively; Fig. 9b). The deviation between experimental and predicted KIEs may, in part, be attributed to errors in entropy calculations; KIE values predicted from DFT calculations solely based on enthalpies (0.82 and

0.31 under dry and wet conditions, respectively) thus not only reflect the decrease in KIE with increasing inlet P_{H2O} but also are closer in experimental values on an absolute scale. Altogether, the reaction mechanism shown in Scheme 3 is in full accord with all steady-state rate measurements under a wide range of conditions, kinetic and thermodynamic effects of H_2O on reaction orders and rates, measured kinetic isotope effects, reversibility-based arguments[12], experimental IR spectra[36], and DFT calculations.

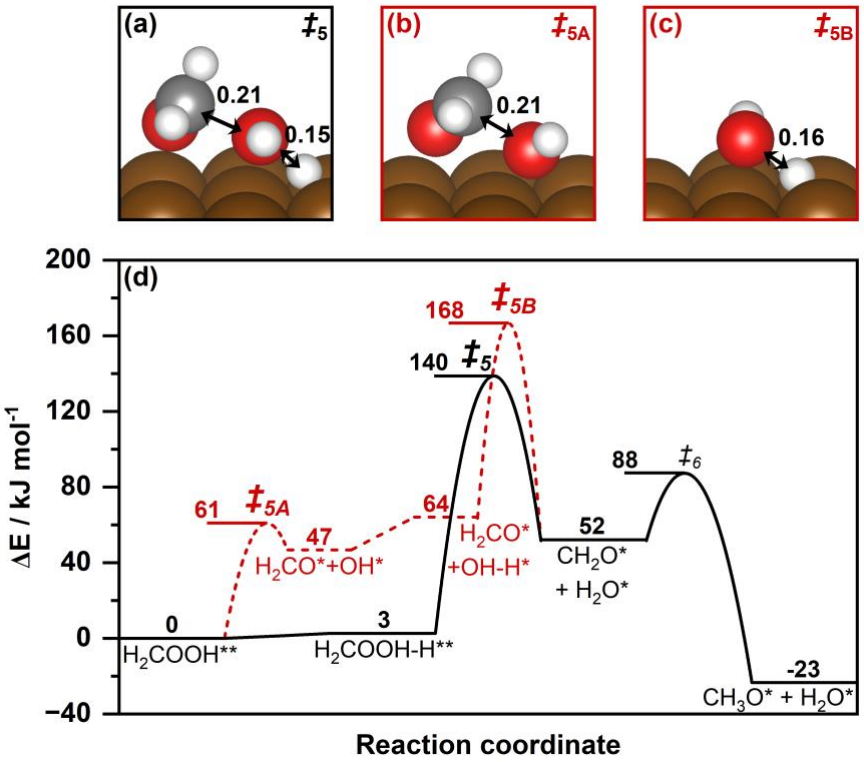

Figure 16. DFT-derived (a-c) geometries of transition states and (d) electronic energy diagram without thermal corrections for steps 4 to 6 of the methanol synthesis cycle as shown in Scheme 3. Distances shown in (a-c) are in the unit of nm. The red-dashed line illustrates the alternative route with sequential C–OH bond cleavage and O–H bond formation for generating H_2O*.

4. Conclusion

Herein, we combine observations from steady-state kinetics, H_2/D_2 isotope effects, microkinetic models, and DFT calculations to elucidate the reaction mechanism of CO_2 hydrogenation on Cu-based catalysts. Methanol synthesis and RWGS on $Cu/ZnO/Al_2O_3$ and

Cu/Al_2O_3 catalyst formulations exhibit identical H_2, CO_2, and H_2O reaction orders, indicating that ZnO does not generate a unique site on $Cu/ZnO/Al_2O_3$ for methanol synthesis that is otherwise absent on Cu/Al_2O_3. Observed invariance in methanol selectivity with changing P_{CO2} and P_{CO} corroborates this finding and illustrates a common active site for methanol synthesis and RWGS. Under methanol synthesis reaction conditions, this active site is saturated by H* and HCOOH** such that the site balance and rate expressions mathematically decouple H_2 and CO_2 dependencies into multiplicative factors, reflecting the observed H_2 and CO_2 reaction orders that are independent of P_{CO2} and P_{H2}, respectively. DFT-derived adsorption energies indicate that the presence of HCOOH** is made possible through favorable H-bonding interactions and the lack of repulsive interaction between HCOOH** and H*. Despite methanol synthesis and RWGS sharing an active site, H_2O preferentially inhibits methanol synthesis rates and impacts only the H_2 reaction order for methanol synthesis. These observations evince the presence of two variable rate-determining steps for methanol synthesis, with H_2O* formation from H_2COOH/H** being rate-determining under dry conditions and CH_2O* hydrogenation to CH_3O* being rate-determining under wet conditions, ultimately leading to disparate H_2 reaction orders and H_2/D_2 kinetic isotope effects under dry and wet conditions. Unequal H_2/D_2 KIEs for methanol synthesis (inverse) and RWGS (negligible) further show the two reactions involve distinct intermediates, congruent with arguments based on reversibility. These findings support a branching reaction network with methanol synthesis following the formate pathway and RWGS following the carboxylate pathway occurring on a common active site, resulting in a kinetic description that accurately reflects measured rates and DFT-derived energies. The proposed mechanism not only highlights the key mechanistic role of high surface coverages in catalytic CO_2 hydrogenation on Cu surfaces but also

motivates the design of Cu surfaces that are less susceptible to water inhibition and more selective in the hydrogenation of formates over carboxylates to enhance methanol yield and selectivity.

5. Acknowledgements

This material is based upon work supported by the National Science Foundation Graduate Research Fellowship under Grant No. 2237827. Financial support was also provided by the University of Minnesota College of Science and Engineering Graduate Fellowship and the U.S. Department of Energy, Office of Basic Energy Science, Catalysis Science Program under Award DE-SC0025321. The work used the Bridges-2 system at the Pittsburgh Supercomputing Center (PSC) through allocation CHM230019 from the Advanced Cyberinfrastructure Coordination Ecosystem: Services & Support (ACCESS) program, which is supported by National Science Foundation under Grants No. 2138259, No. 2138286, No. 2138307, No. 2137603, and No. 2138296. This research used resources of the National Energy Research Scientific Computing Center, a DOE Office of Science User Facility supported by the Office of Science of the U.S. Department of Energy under Contract No. DE-AC02-05CH11231 using NERSC award NERSC DDR-ERCAP0028017. A portion of the research was performed using computational resources sponsored by the Department of Energy's Office of Energy Efficiency and Renewable Energy and located at the National Renewable Energy Laboratory. T.L. acknowledges assistance from Calvin Golimbu for operating the Compact Profile Reactor and Jaideep Singh Soodan for proofreading the manuscript. M.N. thanks the Mines VPRTT Materials Science Graduate Fellowship Program funded by the National Science Foundation award (OAC 2118201).

6. References

[1] G.A. Olah, Towards oil independence through renewable methanol chemistry, Angew. Chemie Int. Ed. 52 (2013) 104–107. https://doi.org/10.1002/anie.201204995.

[2] G.A. Olah, Beyond oil and gas: The methanol economy, Angew. Chemie Int. Ed. 44 (2005) 2636–2639. https://doi.org/10.1002/anie.200462121.

[3] S. Kattel, P. Liu, J.G. Chen, Tuning selectivity of CO_2 hydrogenation reactions at the metal/oxide interface, J. Am. Chem. Soc. 139 (2017) 9739–9754. https://doi.org/10.1021/jacs.7b05362.

[4] S.R. Docherty, C. Copéret, Deciphering metal–oxide and metal–metal interplay via surface organometallic chemistry: A case study with CO_2 hydrogenation to methanol, J. Am. Chem. Soc. 143 (2021) 6767–6780. https://doi.org/10.1021/jacs.1c02555.

[5] A. Beck, M.A. Newton, L.G.A. van de Water, J.A. van Bokhoven, The enigma of methanol synthesis by Cu/ZnO/Al_2O_3-based catalysts, Chem. Rev. 124 (2024) 4543–4678. https://doi.org/10.1021/acs.chemrev.3c00148.

[6] D. Kordus, J. Jelic, M. Lopez Luna, N.J. Divins, J. Timoshenko, S.W. Chee, C. Rettenmaier, J. Kröhnert, S. Kühl, A. Trunschke, R. Schlögl, F. Studt, B. Roldan Cuenya, Shape-dependent CO_2 hydrogenation to methanol over Cu_2O nanocubes supported on ZnO, J. Am. Chem. Soc. 145 (2023) 3016–3030. https://doi.org/10.1021/jacs.2c11540.

[7] S. Kattel, B. Yan, Y. Yang, J.G. Chen, P. Liu, Optimizing binding energies of key intermediates for CO_2 hydrogenation to methanol over oxide-supported copper, J. Am. Chem. Soc. 138 (2016) 12440–12450. https://doi.org/10.1021/jacs.6b05791.

[8] G.C. Chinchen, P.J. Denny, D.G. Parker, M.S. Spencer, D.A. Whan, Mechanism of methanol synthesis from CO_2/CO/H_2 mixtures over copper/zinc oxide/alumina catalysts:

Use of ^{14}C-labelled reactants, App. Catal. 30 (1987) 333–338. https://doi.org/10.1016/S0166-9834(00)84123-8.

[9] K. Klier, V. Chatikavanij, R.G. Herman, G.W. Simmons, Catalytic synthesis of methanol from CO/H_2 IV. The effects of carbon dioxide, J. Catal. 74 (1982) 343–360. https://doi.org/10.1016/0021-9517(82)90040-9.

[10] K.G. Chanchlani, R.R. Hudgins, P.L. Silveston, Methanol synthesis from H_2, CO, and CO_2 over Cu/ZnO catalysts, J. Catal. 136 (1992) 59–75. https://doi.org/10.1016/0021-9517(92)90106-R.

[11] Y. Yang, C.A. Mims, D.H. Mei, C.H.F. Peden, C.T. Campbell, Mechanistic studies of methanol synthesis over Cu from $CO/CO_2/H_2/H_2O$ mixtures: The source of C in methanol and the role of water, J. Catal. 298 (2013) 10–17. https://doi.org/10.1016/j.jcat.2012.10.028.

[12] T.C. Lin, A. Bhan, Rates and reversibility of CO_2 hydrogenation on Cu-based catalysts, J. Catal. 429 (2024) 115214. https://doi.org/10.1016/j.jcat.2023.115214.

[13] T. Vergara, D. Gómez, B. Lacerda de Oliveira Campos, K. Herrera Delgado, R. Jiménez, A. Karelovic, Disclosing the reaction mechanism of CO_2 hydrogenation to methanol over $CuCeO_x/TiO_2$: A combined kinetic, spectroscopic, and isotopic study, ACS Catal. 13 (2023) 14699–14715. https://doi.org/10.1021/acscatal.3c04243.

[14] T.S. Askgaard, J.K. Norskov, C.V. Ovesen, P. Stoltze, A kinetic model of methanol synthesis, J. Catal. 156 (1995) 229–242. https://doi.org/10.1006/jcat.1995.1250.

[15] P.B. Rasmussen, P.M. Holmblad, T. Askgaard, C. V. Ovesen, P. Stoltze, J.K. Norskov, I. Chorkendorff, Methanol synthesis on Cu(100) from a binary gas mixture of CO_2 and H_2, Catal. Lett. 26 (1994) 373–381. https://doi.org/10.1007/BF00810611.

[16] C. V. Ovesen, B.S. Clausen, B.S. Hammershøi, G. Steffensen, T. Askgaard, I. Chorkendorff, J.K. Nørskov, P.B. Rasmussen, P. Stoltze, P. Taylor, A microkinetic analysis of the water-gas shift reaction under industrial conditions, J. Catal. 158 (1996) 170–180. https://doi.org/10.1006/jcat.1996.0016.

[17] M.J.L. Ginés, A.J. Marchi, C.R. Apesteguía, Kinetic study of the reverse water-gas shift reaction over $CuO/ZnO/Al_2O_3$ catalysts, Appl. Catal. A Gen. 154 (1997) 155–171. https://doi.org/10.1016/S0926-860X(96)00369-9.

[18] L.C. Grabow, M. Mavrikakis, Mechanism of methanol synthesis on Cu through CO_2 and CO hydrogenation, ACS Catal. 1 (2011) 365–384. https://doi.org/10.1021/cs200055d.

[19] Y.-F. Zhao, Y. Yang, C. Mims, C.H.F. Peden, J. Li, D. Mei, Insight into methanol synthesis from CO_2 hydrogenation on Cu(111): Complex reaction network and the effects of H_2O, J. Catal. 281 (2011) 199–211. https://doi.org/10.1016/j.jcat.2011.04.012.

[20] M. Behrens, F. Studt, I. Kasatkin, S. Kuhl, M. Havecker, F. Abild-Pedersen, S. Zander, F. Girgsdies, P. Kurr, B.-L. Kniep, M. Tovar, R.W. Fischer, J.K. Norskov, R. Schlogl, The active site of methanol synthesis over $Cu/ZnO/Al_2O_3$ industrial catalysts, Science. 336 (2012) 893–897. https://doi.org/10.1126/science.1219831.

[21] L. Martínez-Suárez, N. Siemer, J. Frenzel, D. Marx, Reaction network of methanol synthesis over Cu/ZnO nanocatalysts, ACS Catal. 5 (2015) 4201–4218. https://doi.org/10.1021/acscatal.5b00442.

[22] E. Fernández-Villanueva, P.G. Lustemberg, M. Zhao, J. Soriano Rodriguez, P. Concepción, M.V. Ganduglia-Pirovano, Water and Cu^+ synergy in selective CO_2 hydrogenation to methanol over $Cu\text{-}MgO\text{-}Al_2O_3$ catalysts, J. Am. Chem. Soc. 146 (2024) 2024–2032. https://doi.org/10.1021/jacs.3c10685.

[23] Y.-F. Shi, P.-L. Kang, C. Shang, Z.-P. Liu, Methanol synthesis from CO_2/CO mixture on Cu–Zn catalysts from microkinetics-guided machine learning pathway search, J. Am. Chem. Soc. 144 (2022) 13401–13414. https://doi.org/10.1021/jacs.2c06044.

[24] E.L. Kunkes, F. Studt, F. Abild-Pedersen, R. Schlögl, M. Behrens, Hydrogenation of CO_2 to methanol and CO on Cu/ZnO/Al_2O_3: Is there a common intermediate or not?, J. Catal. 328 (2015) 43–48. https://doi.org/10.1016/j.jcat.2014.12.016.

[25] P.A. Taylor, P.B. Rasmussen, I. Chorkendorff, Is the observed hydrogenation of formate the rate-limiting step in methanol synthesis?, J. Chem. Soc. Faraday Trans. 91 (1995) 1267. https://doi.org/10.1039/ft9959101267.

[26] K. Takeyasu, Y. Sawaki, T. Imabayashi, S.E.M. Putra, H.H. Halim, J. Quan, Y. Hamamoto, I. Hamada, Y. Morikawa, T. Kondo, T. Fujitani, J. Nakamura, Hydrogenation of formate species using atomic hydrogen on a Cu(111) model catalyst, J. Am. Chem. Soc. 144 (2022) 12158–12166. https://doi.org/10.1021/jacs.2c02797.

[27] W. Tu, P. Ren, Y. Li, Y. Yang, Y. Tian, Z. Zhang, M. Zhu, Y.-H.C. Chin, J. Gong, Y.-F. Han, Gas-dependent active sites on Cu/ZnO clusters for CH_3OH synthesis, J. Am. Chem. Soc. 145 (2023) 8751–8756. https://doi.org/10.1021/jacs.2c13784.

[28] J.-D. Grunwaldt, A.. Molenbroek, N.-Y. Topsøe, H. Topsøe, B.. Clausen, In situ investigations of structural changes in Cu/ZnO catalysts, J. Catal. 194 (2000) 452–460. https://doi.org/10.1006/jcat.2000.2930.

[29] D. Laudenschleger, H. Ruland, M. Muhler, Identifying the nature of the active sites in methanol synthesis over Cu/ZnO/Al_2O_3 catalysts, Nat. Commun. 11 (2020). https://doi.org/10.1038/s41467-020-17631-5.

[30] X. Wang, H. Zhang, Kinetically relevant variation triggered by hydrogen pressure: A

mechanistic case study of CO_2 hydrogenation to methanol over Cu/ZnO, J. Catal. 406 (2022) 145–156. https://doi.org/10.1016/j.jcat.2021.12.034.

[31] J.-F. Portha, K. Parkhomenko, K. Kobl, A.-C. Roger, S. Arab, J.-M. Commenge, L. Falk, Kinetics of methanol synthesis from carbon dioxide hydrogenation over copper–zinc oxide catalysts, Ind. Eng. Chem. Res. 56 (2017) 13133–13145. https://doi.org/10.1021/acs.iecr.7b01323.

[32] G.H. Graaf, E.J. Stamhuis, A.A.C.M. Beenackers, Kinetics of low-pressure methanol synthesis, Chem. Eng. Sci. 43 (1988) 3185–3195. https://doi.org/10.1016/0009-2509(88)85127-3.

[33] G.C. Chinchen, K.C. Waugh, D.A. Whan, The activity and state of the copper surface in methanol synthesis catalysts, Appl. Catal. 25 (1986) 101–107. https://doi.org/10.1016/S0166-9834(00)81226-9.

[34] J. Yoshihara, C.T. Campbell, Methanol synthesis and reverse water–gas shift kinetics over Cu(110) model catalysts: structural sensitivity, J. Catal. 161 (1996) 776–782. https://doi.org/10.1006/jcat.1996.0240.

[35] I.A. Fisher, A.T. Bell, In-situ infrared study of methanol synthesis from H_2/CO_2 over Cu/SiO_2 and $Cu/ZrO_2/SiO_2$, J. Catal. 172 (1997) 222–237. https://doi.org/10.1006/jcat.1997.1870.

[36] Y. Yang, C.A. Mims, R.S. Disselkamp, D. Mei, J.-H. Kwak, J. Szanyi, C.H.F. Peden, C.T. Campbell, Isotope effects in methanol synthesis and the reactivity of copper formates on a Cu/SiO_2 catalyst, Catal. Letters 125 (2008) 201–208. https://doi.org/10.1007/s10562-008-9592-4.

[37] T.C. Lin, U. De La Torre, A. Hejazi, S. Kwon, E. Iglesia, Unimolecular and bimolecular

formic acid decomposition routes on dispersed Cu nanoparticles, J. Catal. 404 (2021) 814–831. https://doi.org/10.1016/j.jcat.2021.08.049.

[38] P. Kampe, N. Herrmann, C. Ruhmlieb, M. Finsel, O. Korup, R. Horn, J. Albert, Spatially resolved reaction profiles of CO_2 hydrogenation to methanol using In-based catalysts in a compact profile reactor, ACS Sustain. Chem. Eng. (2024). https://doi.org/10.1021/acssuschemeng.4c03279.

[39] S. Sichert, S.-F. Stahl, O. Korup, R. Horn, Measuring adsorbate profiles in heterogeneous catalytic reactors by iso-potential operando DRIFTS applied to CO_2 methanation on Ni, ACS Catal. 14 (2024) 8676–8693. https://doi.org/10.1021/acscatal.4c00536.

[40] W.M. Haynes, D.R. Lide, T.J. Bruno, CRC handbook of chemistry and physics, 97th ed., CRC Press, Boca Raton, FL, 2016. https://doi.org/10.1201/9781315380476.

[41] N. Ray, V.K. Rastogi, D.S. Chhabra, S. Dutt, S.P. Sen, Deactivation of low temperature shift catalyst: Part II poisoning by chlorine, J. Res. Inst. Catal., Hokkaido Univ. 30 (1982) 25–37.

[42] K. Larmier, S. Tada, A. Comas-Vives, C. Copéret, Surface sites in Cu-nanoparticles: Chemical reactivity or microscopy?, J. Phys. Chem. Lett. 7 (2016) 3259–3263. https://doi.org/10.1021/acs.jpclett.6b01328.

[43] T. Holm, Mechanism of the flame ionization detector II. Isotope effects and heteroatom effects, J. Chromatogr. A 782 (1997) 81–86. https://doi.org/10.1016/S0021-9673(97)00483-4.

[44] N.B. Vargaftik, N.A. Vanicheva, Thermal conductivity of some deuterated compounds in the gaseous phase, J. Eng. Phys. 27 (1974) 978–981. https://doi.org/10.1007/BF00861605.

[45] G. Kresse, J. Furthmüller, Efficient iterative schemes for ab initio total-energy

calculations using a plane-wave basis set, Phys. Rev. B 54 (1996) 11169–11186. https://doi.org/10.1103/PhysRevB.54.11169.

[46] G. Kresse, J. Furthmüller, Efficiency of ab-initio total energy calculations for metals and semiconductors using a plane-wave basis set, Comput. Mater. Sci. 6 (1996) 15–50. https://doi.org/10.1016/0927-0256(96)00008-0.

[47] K. Momma, F. Izumi, VESTA 3 for three-dimensional visualization of crystal, volumetric and morphology data, J. Appl. Crystallogr. 44 (2011) 1272–1276. https://doi.org/10.1107/S0021889811038970.

[48] J.P. Perdew, K. Burke, M. Ernzerhof, Generalized gradient approximation made simple, Phys. Rev. Lett. 77 (1996) 3865–3868. https://doi.org/10.1103/PhysRevLett.77.3865.

[49] Z. Li, N. Li, N. Wang, B. Zhou, P. Yin, B. Song, J. Yu, Y. Yang, Mechanism investigations on water gas shift reaction over Cu(111), Cu(100), and Cu(211) surfaces, ACS Omega 7 (2022) 3514–3521. https://doi.org/10.1021/acsomega.1c05991.

[50] X. Wang, H. Zhang, H. Qin, K. Wu, K. Wang, J. Ma, W. Fan, A DFT study of methanol synthesis from CO_2 hydrogenation on Cu/ZnO catalyst, Fuel 346 (2023) 128381. https://doi.org/10.1016/j.fuel.2023.128381.

[51] D. Kopač, B. Likozar, M. Huš, Catalysis of material surface defects: Multiscale modeling of methanol synthesis by CO_2 reduction on copper, Appl. Surf. Sci. 497 (2019) 143783. https://doi.org/10.1016/j.apsusc.2019.143783.

[52] S. Grimme, S. Ehrlich, L. Goerigk, Effect of the damping function in dispersion corrected density functional theory, J. Comput. Chem. 32 (2011) 1456–1465. https://doi.org/10.1002/jcc.21759.

[53] G. Kresse, D. Joubert, From ultrasoft pseudopotentials to the projector augmented-wave

method, Phys. Rev. B 59 (1999) 1758–1775. https://doi.org/10.1103/PhysRevB.59.1758.

[54] R. Tran, Z. Xu, B. Radhakrishnan, D. Winston, W. Sun, K.A. Persson, S.P. Ong, Surface energies of elemental crystals, Sci. Data 3 (2016) 160080. https://doi.org/10.1038/sdata.2016.80.

[55] H.J. Monkhorst, J.D. Pack, Special points for Brillouin-zone integrations, Phys. Rev. B 13 (1976) 5188–5192. https://doi.org/10.1103/PhysRevB.13.5188.

[56] N. Barrow, J. Bradley, B. Corrie, Y. Cui, T.D. Tran, T.E. Erden, A. Fish, M. Garcia, P. Glen, N. Mistry, M. Nicholson, S. Roloff-Standring, D. Sheldon, T. Smith, A. Summer, K.U. Din, N. Macleod, Doubling the life of Cu/ZnO methanol synthesis catalysts via use of Si as a structural promoter to inhibit sintering, Sci. Adv. 10 (2024) 1–11. https://doi.org/10.1126/sciadv.adk2081.

[57] M.B. Fichtl, D. Schlereth, N. Jacobsen, I. Kasatkin, J. Schumann, M. Behrens, R. Schlögl, O. Hinrichsen, Kinetics of deactivation on Cu/ZnO/Al_2O_3 methanol synthesis catalysts, Appl. Catal. A Gen. 502 (2015) 262–270. https://doi.org/10.1016/j.apcata.2015.06.014.

[58] X. Liu, H. Wang, J. Lu, Recent progress in understanding the nature of active sites for methanol synthesis over Cu/ZnO catalysts, J. Catal. 436 (2024) 115561. https://doi.org/10.1016/j.jcat.2024.115561.

[59] D. Sheppard, R. Terrell, G. Henkelman, Optimization methods for finding minimum energy paths, J. Chem. Phys. 128 (2008). https://doi.org/10.1063/1.2841941.

[60] G. Henkelman, H. Jónsson, A dimer method for finding saddle points on high dimensional potential surfaces using only first derivatives, J. Chem. Phys. 111 (1999) 7010–7022. https://doi.org/10.1063/1.480097.

[61] G. Henkelman, G. Jóhannesson, H. Jónsson, Methods for finding saddle points and

minimum energy paths, in: Theor. Methods Condens. Phase Chem., Kluwer Academic Publishers, Dordrecht, n.d.: pp. 269–302. https://doi.org/10.1007/0-306-46949-9_10.

[62] T. Frederiksen, M. Paulsson, M. Brandbyge, A.-P. Jauho, Inelastic transport theory from first principles: Methodology and application to nanoscale devices, Phys. Rev. B 75 (2007) 205413. https://doi.org/10.1103/PhysRevB.75.205413.

[63] P. Deshlahra, J. Conway, E.E. Wolf, W.F. Schneider, Influence of dipole–dipole interactions on coverage-dependent adsorption: CO and NO on Pt(111), Langmuir 28 (2012) 8408–8417. https://doi.org/10.1021/la300975s.

[64] E.B. Wilson, J.C. Decius, P.C. Cross, Molecular vibrations: The theory of infrared and raman vibrational spectra, McGraw-Hill Book Company, Inc.; Dover Publications, Inc., New York, 1980.

[65] Donald A. McQuarrie, Statistical mechanics, University Science Books, Sausalito, CA, 2000.

[66] W. Wang, Z. Qu, L. Song, Q. Fu, Probing into the multifunctional role of copper species and reaction pathway on copper-cerium-zirconium catalysts for CO2 hydrogenation to methanol using high pressure in situ DRIFTS, J. Catal. 382 (2020) 129–140. https://doi.org/10.1016/j.jcat.2019.12.022.

[67] M. Santiago, K. Barbera, C. Ferreira, D. Curulla-Ferré, P. Kolb, J. Pérez-Ramírez, By-product co-feeding reveals insights into the role of zinc on methanol synthesis catalysts, Catal. Commun. 21 (2012) 63–67. https://doi.org/10.1016/j.catcom.2012.01.031.

[68] J. Thrane, S. Kuld, N.D. Nielsen, A.D. Jensen, J. Sehested, J.M. Christensen, Methanol-assisted autocatalysis in catalytic methanol synthesis, Angew. Chemie Int. Ed. 59 (2020) 18189–18193. https://doi.org/10.1002/anie.202006921.

[69] R.D. Johnson III, ed., NIST Computational Chemistry Comparison and Benchmark Database, NIST Standard Reference Database Number 101 Release 22, May, 2022. https://doi.org/10.18434/T47C7Z.

[70] I. Nakamura, H. Nakano, T. Fujitani, T. Uchijima, J. Nakamura, Evidence for a special formate species adsorbed on the Cu–Zn active site for methanol synthesis, Surf. Sci. 402–404 (1998) 92–95. https://doi.org/10.1016/S0039-6028(97)00910-2.

[71] F.C. Meunier, I. Dansette, A. Paredes-Nunez, Y. Schuurman, Cu-bound formates are main reaction intermediates during CO_2 hydrogenation to methanol over Cu/ZrO_2, Angew. Chemie Int. Ed. 62 (2023). https://doi.org/10.1002/anie.202303939.

[72] Y. Yang, C.A. Mims, R.S. Disselkamp, J.-H. Kwak, C.H.F. Peden, C.T. Campbell, (Non)formation of methanol by direct hydrogenation of formate on copper catalysts, J. Phys. Chem. C 114 (2010) 17205–17211. https://doi.org/10.1021/jp104068k.

[73] P. Wu, B. Yang, Significance of surface formate coverage on the reaction kinetics of methanol synthesis from CO_2 hydrogenation over Cu, ACS Catal. 7 (2017) 7187–7195. https://doi.org/10.1021/acscatal.7b01910.

[74] S. Kattel, P.J. Ramírez, J.G. Chen, J.A. Rodriguez, P. Liu, Active sites for CO_2 hydrogenation to methanol on Cu/ZnO catalysts, Science. 355 (2017) 1296–1299. https://doi.org/10.1126/science.aal3573.

[75] D. Xu, P. Wu, B. Yang, Essential role of water in the autocatalysis behavior of methanol synthesis from CO_2 hydrogenation on Cu: A combined DFT and microkinetic modeling study, J. Phys. Chem. C 123 (2019) 8959–8966. https://doi.org/10.1021/acs.jpcc.8b12460.

[76] J. Nakamura, J.M. Campbell, C.T. Campbell, Kinetics and mechanism of the water-gas shift reaction catalysed by the clean and Cs-promoted Cu(110) surface: a comparison with

Cu(111), J. Chem. Soc. Faraday Trans. 86 (1990) 2725. https://doi.org/10.1039/ft9908602725.

[77] E. Lam, K. Larmier, P. Wolf, S. Tada, O. V. Safonova, C. Copéret, Isolated Zr surface sites on silica promote hydrogenation of CO_2 to CH_3OH in supported Cu catalysts, J. Am. Chem. Soc. 140 (2018) 10530–10535. https://doi.org/10.1021/jacs.8b05595.

[78] G. Noh, S.R. Docherty, E. Lam, X. Huang, D. Mance, J.L. Alfke, C. Copéret, CO_2 hydrogenation to CH_3OH on supported Cu nanoparticles: Nature and role of Ti in bulk oxides vs isolated surface sites, J. Phys. Chem. C 123 (2019) 31082–31093. https://doi.org/10.1021/acs.jpcc.9b09631.

[79] F. Studt, F. Abild-Pedersen, Q. Wu, A.D. Jensen, B. Temel, J.-D. Grunwaldt, J.K. Nørskov, CO hydrogenation to methanol on Cu–Ni catalysts: Theory and experiment, J. Catal. 293 (2012) 51–60. https://doi.org/10.1016/j.jcat.2012.06.004.

[80] A.A. Gokhale, J.A. Dumesic, M. Mavrikakis, On the mechanism of low-temperature water gas shift reaction on copper, J. Am. Chem. Soc. 130 (2008) 1402–1414. https://doi.org/10.1021/ja0768237.

[81] N.K. Razdan, T.C. Lin, A. Bhan, Concepts relevant for the kinetic analysis of reversible reaction systems, Chem. Rev. 123 (2023) 2950–3006. https://doi.org/10.1021/acs.chemrev.2c00510.